Gallaher, SG et al 2017 Field observations and results of a 1-D boundary layer model for developing near-surface temperature maxima in the Western Arctic. *Elem Sci Anth,* 5: 11, pp. 1–21, DOI: https://doi.org/10.1525/elementa.195

RESEARCH ARTICLE

Field observations and results of a 1-D boundary layer model for developing near-surface temperature maxima in the Western Arctic

Shawn G. Gallaher*, Timothy P. Stanton§, William J. Shaw§, Sung-Ho Kang†, Joo-Hong Kim† and Kyoung-Ho Cho†

Summer sea ice extent in the Western Arctic has decreased significantly in recent years resulting in increased solar input into the upper ocean. Here, a comprehensive set of *in situ* shipboard, on-ice, and autonomous ice-ocean measurements were made of the early stages of formation of the near-surface temperature maximum (NSTM) in the Canada Basin. These observations along with the results from a 1-D turbulent boundary layer model indicate that heat storage associated with NSTM formation is largely due to the absorption of penetrating solar radiation just below a protective summer halocline. The depth of the summer halocline was found to be the most important factor for determining the amount of solar radiation absorbed in the NSTM layer, while halocline strength controlled the amount of heat removed from the NSTM by turbulent transport. Observations using the Naval Postgraduate School Turbulence Frame show that the NSTM was able to persist despite periods of intermittent turbulence because transport rates were too small to remove significant amounts of heat from the NSTM layer. The development of the early and late summer halocline and NSTM were found to be linked to summer season buoyancy and wind events. For the early summer NSTM, 1-D boundary layer model results show that melt pond drainage provides sufficient buoyancy to the summer halocline to prevent subsequent wind events from mixing out the NSTM. For the late summer NSTM, limited freshwater inputs reduce the strength of the summer halocline making the balance between interfacial stresses and buoyancy more tenuous. As a result, the late summer NSTM is an ephemeral feature dependent on local wind conditions, while the early summer NSTM is more persistent and able to store heat in the near-surface ocean beyond the summer season.

Keywords: Near-surface temperature maximum; Local turbulence closure model; Turbulent fluxes

1. Introduction

Recent changes in the Arctic ice-ocean system have led to an increase in upper ocean heating. The primary source of this heating is the two-fold rise in ocean-absorbed solar radiation (Perovich et al., 2007) that results from rapidly declining summer sea ice extent (Comiso et al., 2008; Steele et al., 2010). Recent studies in the Canada Basin show that this absorbed solar heating is partitioned 0.23/0.77 between ocean heat storage and latent heat loss (basal ice melt), respectively (Toole et al., 2010; Gallaher et al., 2016). Most of the oceanic heat is accumulated in near-surface temperature maximum (NSTM) features. The NSTM is defined as an upper ocean (< 50 m) temperature maximum that: 1) is at least 0.2°C above freezing (δT); 2) has a salinity < 31; and 3) resides above a cooler water layer by at least 0.1°C (Jackson et al., 2010).

* United States Naval Academy, Annapolis, Maryland, US

§ Naval Postgraduate School, Monterey, California, USA

† Korea Polar Research Institute, Incheon, KR

Corresponding author: Shawn Gallaher (sggallah1@nps.edu)

Jackson et al. (2010) attribute NSTM development to the absorption of solar radiation in shallow, stratified layers beneath melting sea ice and open water during summer. Steele et al. (2011) present an additional formation process caused by cooling of the near-surface ocean under open water areas in late summer, which leaves behind a warmer subsurface layer. Although NSTM heat is gained in the summer, the release of this heat often occurs in later seasons. Observations in the Canada Basin show that the NSTM often survives into fall, and that heat from this layer can be mixed into the surface mixed layer to delay or slow freeze up (Steele et al., 2008; Jackson et al., 2010; 2012; Steele et al., 2011; Timmermans, 2015).

Early studies of the NSTM during AIDJEX (Maykut and McPhee, 1995) and SHEBA (McPhee et al., 1998) found that the layer was present directly below the summer surface mixed layer, at depths between 25 and 35 m. However, the Canada Basin upper ocean is freshening (McPhee et al., 2009) through a combination of sea ice melt, river runoff, and convergence of Ekman boundary layer transports under the Beaufort Gyre (MacDonald et al., 1999;

Proshutinsky et al., 2009; Yamamoto-Kawai et al., 2009). This freshening decreases the thickness of the surface mixed layer as turbulent length scales decrease under the effects of stabilizing buoyancy fluxes (McPhee, 1994). In the current century, the base of the summer surface mixed layer has shoaled to an average depth of 16 m (Toole et al., 2010), and the salinity of the NSTM has freshened by 4 and its temperature warmed by 1.5°C (Jackson et al., 2011). To anticipate how these changes in upper ocean properties will affect heat storage in the Canada Basin requires an understanding of the processes that form and sustain the NSTM.

In previous studies, the NSTM has been examined primarily from a seasonal evolution and interannual variability perspective. However, comprehensive, *in situ* observations of a developing NSTM have not, to date, been made. In this study, we used data from the Office of Naval Research (ONR) Marginal Ice Zone (MIZ) field program and the 2014 Korea Polar Research Institute (KOPRI) Arctic summer cruise along with a one-dimensional (1-D) turbulent boundary layer model to investigate NSTM formation. We had three objectives: 1) determine the relative contributions of solar radiative forcing, buoyancy forcing, and shear-generated turbulent processes to the development of the NSTM; 2) identify atmosphere-ice-ocean system events that initiate NSTM development; and 3) establish factors that affect NSTM survivability. In the first part of this paper, we focus on the processes that form and preserve/erode the late summer NSTM. We then compare these findings to a modeling study of the early summer NSTM that formed at the location of another MIZ experiment.

2. In situ observations

2.1 Marginal Ice Zone experiment

The bulk of the observations used in this study were collected during the 2014 ONR MIZ experiment in the Canada Basin (see Lee et al., 2012, for a program description). Five autonomous, ice-based, multi-instrument "clusters" were deployed to collect a wide range of ice and ocean data throughout the spring and summer. Clusters 1–4 were deployed in early spring along the 135°W meridian in the eastern Canada Basin (**Figure 1a**) from small air-supported ice camps. Cluster 5 (C5) was deployed in late summer, further north, at the edge of the seasonal ice zone (**Figure 1a**) from the KOPRI icebreaker *Araon* (R/V *Araon*). Coincident with the C5 deployment, a joint MIZ-KOPRI Ice Camp was established between year days (YDs) 221 and 226 (9–14 August) to make intensive manned observations of the air-ice-ocean system. Data from the MIZ-KOPRI Ice Camp and the C5 autonomous instruments form the main focus of this work; however, supplemental data from MIZ cluster 2 (C2) were included to model the NSTM that developed in early summer.

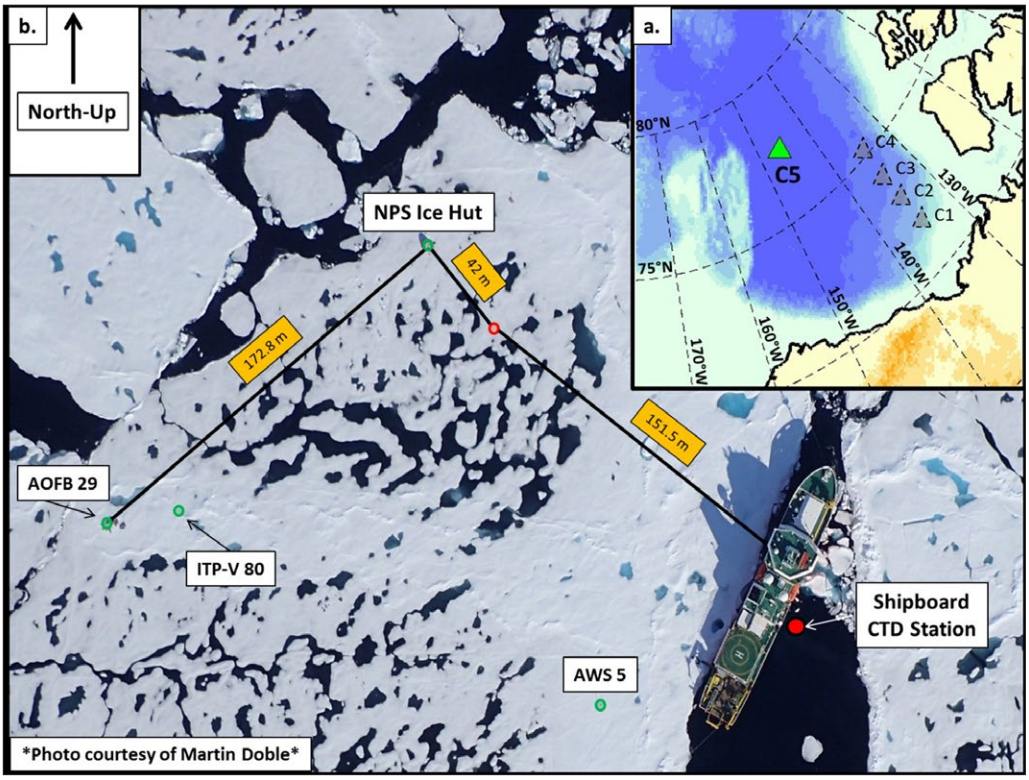

Figure 1: The ONR-KOPRI Ice Camp at MIZ Cluster 5. (a) Topo-bathymetric map of the Canada Basin showing the location of the joint ONR-KOPRI Ice Camp at MIZ Cluster 5 (C5, green triangle) between 9 and 14 August 2014. Also shown are the initial positions of MIZ Clusters 1–4 deployed in early spring (gray triangles). **(b)** Image of the ONR-KORPI Ice Camp taken from a Maritime Helicopters BELL 206 at 600 m. Ice Camp image is annotated with the locations of the on-ice instruments to include the Autonomous Ocean Flux Buoy (AOFB) 29, Automated Weather Station (AWS) 5, the R/V *Araon* CTD station, Ice-tethered Profiler – velocity 80 (ITP-V 80), and NPS Ice Hut used to deploy the Turbulence Frame. DOI: https://doi.org/10.1525/elementa.195.f1

2.2 Data sources

The air-ice-ocean observations at C5 came from shipboard and on-ice instruments (**Figures 1b** and **2**). Starting on the air-side, surface winds were measured by an RM Young anemometer on the Scottish Association of Marine Science Automated Weather System 5 (AWS 5) and a Vaisala Multi-Weather System on Autonomous Ocean Flux Buoy 29 (AOFB 29). Fluxes of downgoing shortwave radiation were measured by an Apogee SP-110 pyranometer on AWS 5 and a Hukseflux SR03 pyranometer on AOFB 29. AOFB 29 was not deployed until YD 224; therefore, hourly AWS 5 data were used between YDs 221.8 and 224, and an average of the 1-h AWS 5 and the linearly interpolated 15-min AOFB 29 anemometer and pyranometer data were used between YD 224 and YD 225.8. AOFB 29 was also equipped with a Thies Clima 3-D sonic anemometer that provided estimates of air-ice wind stress every 3 h. All of the meteorological sensors were mounted approximately 2 m above the sea ice surface.

In the ice, a 16-element, 30-cm spacing temperature string on the AOFB measured thermal gradients in the sea ice and the near-surface ocean. Along with these *in situ* in-ice measurements, surface-ice conditions were observed remotely using declassified visible grayscale satellite images at 1-m resolution. These images were analyzed to characterize open water, sea ice, and melt pond areal coverage in the vicinity of C5. Visible imagery for this study is available on the Global Fiducials Library of the U. S. Geological Survey (http://gfl.usgs.gov/gallery_main.shtml?current=4).

In the ocean, observations of turbulent processes in the ice-ocean boundary layer (IOBL) were made from the Naval Postgraduate School (NPS) Turbulence Frame, which was deployed through a 0.6 m hydro-hole beneath the NPS Ice Hut located ~ 200 m from the R/V *Araon* (**Figure 1b**). In addition to this 200-m buffer, the location of the NPS Ice Hut was chosen based on the prevailing winds (from the north) to avoid turbulent contamination from the ship and to capture the along-floe drag characteristics at MIZ C5. The frame was equipped with two custom-built ocean flux packages, consisting of (with accuracies) a 4-path, three-dimensional acoustic travel-time current meter (ACM) (± 0.25 mm s^{-1} RMS noise level), a free-flushing inductive conductivity cell (± 0.002 mS cm^{-1}), and a fast low-noise thermistor (± 1 mC). These sensors, sampled at 4 Hz, are mechanically integrated to form a 0.001 m^{-3} sample volume (for full flux package description, see Shaw et al., 2008, and the AOFB program website, http://www.oc.nps.edu/~stanton/fluxbuoy/index.html). The flux packages, fp1 (top) and fp2 (bottom), were mounted on each end of a 6-m vertical frame (**Figure 2**). The frame instruments ran continuously between YDs 221.8 and 225.8 during which the frame was repositioned in the vertical, by an electric winch, to straddle the base of the surface mixed layer. This sampling strategy allowed for the direct observation of turbulent parameters just above and within the surface mixed layer pycnocline. A third flux package, at a fixed depth of about 2.5 m below the ice base (~ 4.5-m depth), was mounted on AOFB 29 with the same specifications described above, except at a 2-Hz sampling frequency.

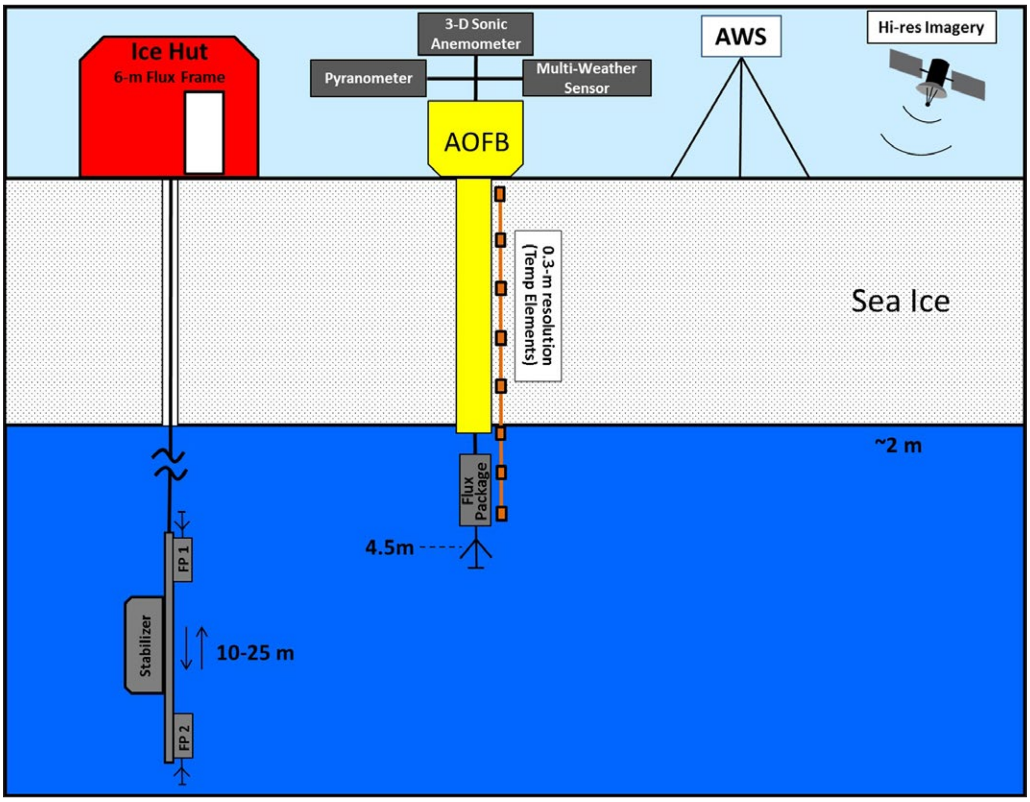

Figure 2: MIZ Cluster 5 sensors. Sensor schematic (vertical view) of the on-ice deployed instruments at the MIZ-KOPRI Ice Camp shown on Figure 1b. DOI: https://doi.org/10.1525/elementa.195.f2

In situ salinity and temperature profiles at MIZ C5 were obtained from R/V *Araon* CTD measurements (SeaBird SBE 911 plus), which were conducted in a lead located off the starboard side of the ship (see **Figure 1b**). CTD profiles between 1 and 600 m were taken every 2 h during the 4-day Ice Camp study period. For the modeling study conducted at MIZ C2, salinity and temperature data were provided by AOFB 33 and Ice-Tethered Profiler 77 (ITP 77) (Krishfield et al., 2008; Toole et al., 2011). Data from AOFB 33 were observed at a fixed depth of 4.5 m, while ITP 77 provided profiled data between 7 and 250 m every 3 h at 1-m resolution. On the same instrument, at a fixed depth of 6 m, a MicroCAT sensor sampled salinity and temperature every 15 min.

2.3 Defining the early and late summer NSTMs

The CTD profiles from R/V *Araon* reveal that two NSTMs were present in the surface ocean (< 35 m) during the last two days of the MIZ-KOPRI Ice Camp. These features, at about 25 m and 10 m (**Figure 3c**), were found at depths with increased halocline stratification (**Figure 3a–b**). The 25-m depth feature will be referred to as the early summer NSTM, as its depth corresponds well with the August depths of the NSTMs observed at MIZ clusters 2–4, which developed in early July (Gallaher et al., 2016). The 10-m feature will be referred to as the late summer NSTM, given that it developed during the late summer observation period, around YD 224 (12 August). The early summer NSTM had a strong temperature maximum ($\delta T = \sim 0.5°C$) and easily met the Jackson et al. (2010) NSTM criteria; however, the late summer NSTM was much cooler and did not meet these criteria. The disparity in temperature between these two NSTMs was due to the differences in residence time in the upper ocean. The early summer NSTM formed in early July under heavily ponded sea ice and high sun angles exposing the upper ocean to significant amounts of solar insolation for more than a month prior to the study period. Conversely, the late summer NSTM formed during the study period under high ice concentration and lower sun angles limiting solar input to the surface mixed layer. Therefore, in order to maintain the spirit of the NSTM definition by Jackson et al. (2010), the temperature above freezing criterion was relaxed to $\delta T > 0.17°C$ for the late summer NSTM. Upper ocean haloclines associated with the early and late summer NSTMs will be likewise referred to as the early and late summer haloclines (**Figure 3a–b**).

2.4 NSTM heat content and upper ocean freshwater storage

To investigate NSTM development, we tracked changes in upper ocean heat content, stratification, and freshwater content that occurred in response to radiative, buoyancy, and dynamic forcing. The heat content of the late summer NSTM layer was calculated as

$$Q_{oml} = c_p \rho_{sw} \int_{z_2}^{z_1} \delta T(s,p)\,dz, \tag{1}$$

where c_p is the specific heat of seawater (3986 J kg^{-1} K^{-1}), ρ_{sw} is the reference density (1022 kg m^{-3}) of the upper ocean, and δT is the temperature above the local freez-

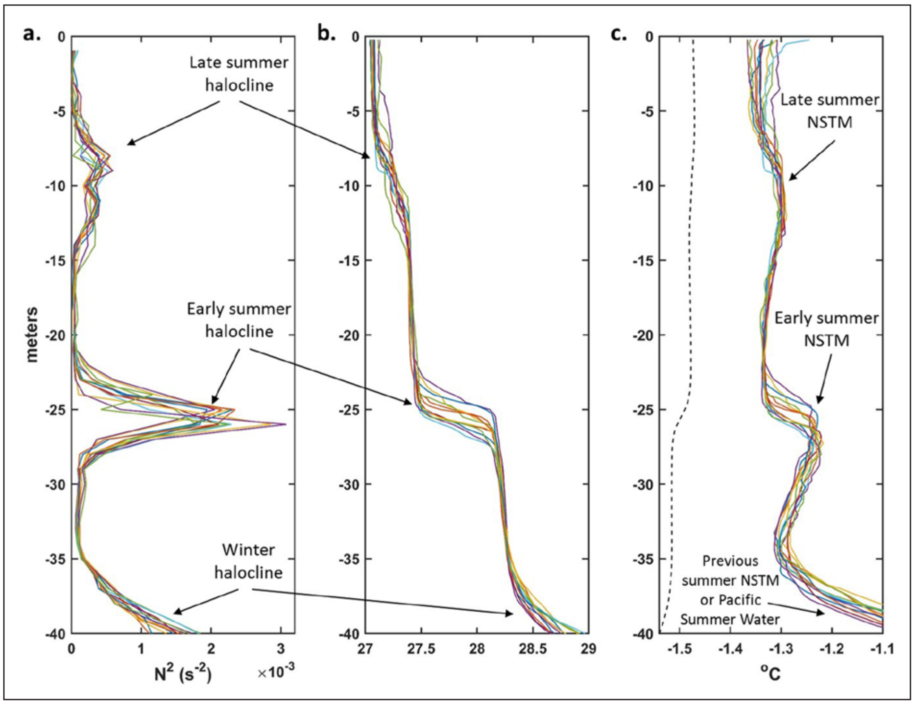

Figure 3: Defining the early and late summer haloclines and near-surface temperature maximum. R/V *Araon* CTD profiles of **(a)** N^2, **(b)** salinity, and **(c)** temperature for the last two days of the MIZ-KOPRI Ice Camp (YDs 223.8–225.8). Black dashed line in Figure 3c shows the average freezing temperature with depth. Peaks in temperature and stratification highlight the respective levels of the early and late summer haloclines and the near-surface temperature maximum (NSTM) for early and late summer and the previous summer. DOI: https://doi.org/10.1525/elementa.195.f3

ing temperature which was integrated over the control volume between depths z_1 and z_2. For this time series, the control volume for the late summer NSTM layer was defined as the average observed NSTM depth (12 m) plus or minus 5 m (7–17 m).

To track the summer halocline we used the depth of the maximum, near-surface buoyancy frequency following the first appearance of the NSTM,

$$N^2_{\max} = -\frac{g}{\rho_o}\frac{d\rho}{dz}_{\max}, \tag{2}$$

where $d\rho/dz$ is the potential density gradient and g is the gravitational acceleration (9.81 m s^{-1}).

Freshwater storage was calculated to determine the amount of buoyancy added to the near-surface ocean and to estimate the total (i.e., from basal, surface, and lateral melting) amount of freshwater input from the sea ice. Choice of the appropriate control volume for this calculation was a challenge since the surface freshwater inputs were in close proximity to the early summer halocline (~ 25 m). As a result, application of a constant depth control volume was not suitable as surface freshwater was mixed below and/or entrained salt was mixed above the lower boundary of the control volume during wind events. Therefore, a variable depth control volume was used based on the 1022 kg m^{-3} isopycnal near the base of the surface mixed layer (magenta line on **Figure 4b**). To calculate surface freshwater input, we used the freshwater content equation (Rudels et al., 2004; Proshutinsky et al., 2009)

$$FWC = \int_{z_2}^{z_1} \frac{[S_{ref} - S(z)]}{S_{ref}} dz, \tag{3}$$

where S_{ref} is reference salinity (27.5), $S(z)$ is the salinity at water depth z, and z_1 and z_2 are the upper (1 m) and lower (1022 kg m^{-3} isopycnal) boundaries of the FWC control volume. All salinity data were processed using the Practical Salinity Scale 1978 (Fofonoff and Millard, 1983).

2.5 One-dimensional analysis of NSTMs

The 2014 ONR MIZ experiment was one of the largest observational programs ever carried out in the Western Arctic; nevertheless, most of the data collected came from widely dispersed single point autonomous platforms moored to drifting ice floes. Drift speeds were ~ 10 km day^{-1}, limiting observations to a largely temporal view of the upper ocean. Previous work by Timmermans et al. (2012) show that the Canada Basin surface mixed layer can have significant horizontal density gradients during the winter season; however, the findings of Gallaher et al. (2016) indicate remarkable regional consistency in salinity and temperature profiles across the upper 50 m of the ocean during the summer season (see Figure 15 of Gallaher et al., 2016). Heat budgets conducted during this study closed to within about 10%, suggesting that lateral advections were very low and that the bulk of upper ocean heat storage gains and basal ice melt were achieved by absorption of local shortwave radiative input.

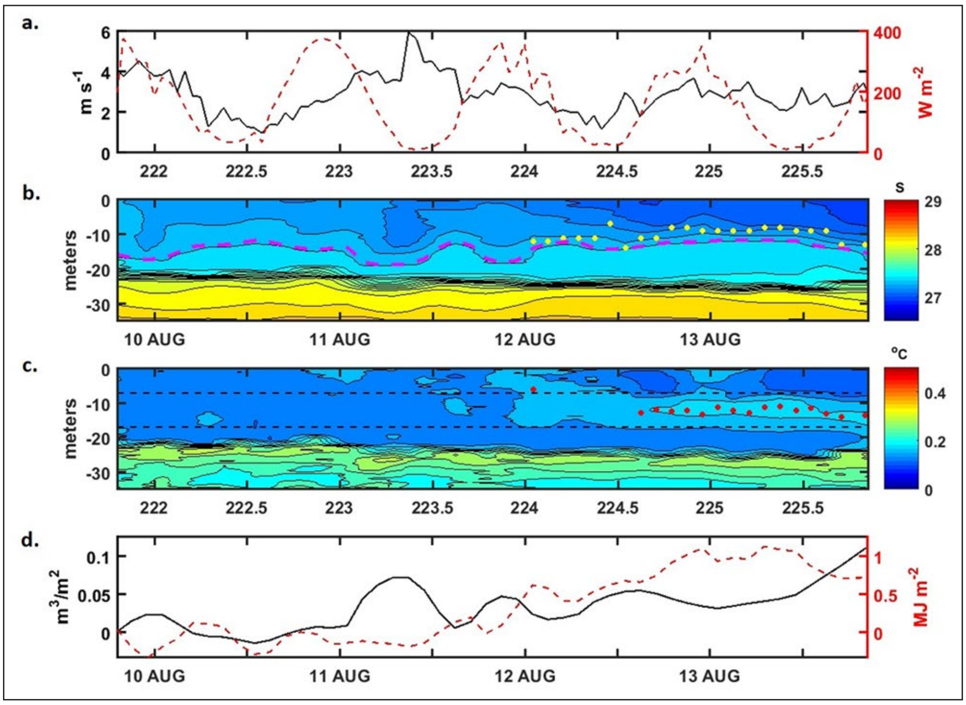

Figure 4: CTD observations from R/V *Araon.* (a) 2-m wind speed (black line) and incoming solar radiation from AWS 5 and AOFB 29 (dotted red line). **(b)** Salinity (S) collected from R/V *Araon* CTD casts binned every 0.25 m with the near-surface N^2 maximum (yellow dots) and 1022 kg m^{-3} isopycnal (dashed magenta line) overlaid to show the lower integration limit for freshwater content calculations (FWC). **(c)** 0.25-m binned temperature above freezing data with depth of the late summer NSTM (red dots) and NSTM layer control volume (enclosed by black dashed lines). **(d)** Cumulative FWC (black line) in the surface mixed layer and cumulative heat storage (red dashed line) in the NSTM layer. DOI: https://doi.org/10.1525/elementa.195.f4

Likewise, Jackson et al. (2010) demonstrated the year-to-year reoccurrence of the summer halocline and NSTM in the Canada Basin at depths between 10 and 30 m during the 2002–2007 melt seasons. The ubiquitous nature of the summer halocline and NSTM in the Canada Basin suggests that these features are generated by vertical and not horizontal advective processes. Given these summer observations, we conducted a 1-D investigation of NSTM development using point source observations and a local turbulent boundary layer model.

3. Local turbulence closure (LTC) model

3.1 Similarity based closure and flux calculations

To fill in observational gaps and to better understand the dynamics responsible for development of the NSTM, we employed the McPhee (1999; 2008) Local Turbulence Closure (LTC) model. The basic premise behind the LTC modeling approach is that vertical profiles of turbulent mixing length (λ) may be determined using similarity scaling that accounts for rotational and buoyancy effects on the IOBL (McPhee et al., 1987). The eddy viscosity (K_m) and eddy diffusion ($K_{h/s}$) terms in the first-order closure equations are then determined from the product of λ with the local friction scale velocity ($u*$). Estimates of turbulent flux are then obtained from the product of these diffusivities with the local gradients of velocity, temperature, and salinity. LTC model kinematic fluxes were calculated through the following relationship

$$<w'x'> = -K_x \nabla_z \mathrm{x}, \tag{4}$$

where w' is the vertical velocity perturbation, x' is the scalar (T, S) or horizontal vector (u,v) perturbations, and K is the eddy diffusivity (K_h or K_s) or eddy viscosity (K_m). Dynamic heat fluxes were calculated by

$$F_H = c_p \rho_{sw} \langle w'T' \rangle. \tag{5}$$

Kinematic salt fluxes ($<w'S'>$) were converted to buoyancy fluxes to identify vertical layers where the turbulent redistribution of fresher water enhanced local buoyancy. Buoyancy fluxes ($<w'b'>$) were calculated by

$$<w'b'> = \frac{g}{\rho_{sw}} \langle w'\rho' \rangle, \tag{6}$$

where ρ' is the density perturbation derived from local density changes associated with kinematic salt and heat fluxes in the equation of state.

To estimate the depth of the actively mixing ice-ocean boundary layer (IOBL) in the LTC model, the bulk Richardson number (Ri_{bulk}) is calculated by (e.g., Large et al., 1994)

$$Ri_{bulk} = \frac{g(\Delta\rho)}{\rho_{sw}\left[(\Delta u)^2 + (\Delta v)^2\right]} \Delta h, \tag{7}$$

where $\Delta\rho$, Δu, and Δv are the changes in density and horizontal velocity across a water thickness Δh. Δu and Δv were calculated by taking the difference of the LTC upper ocean velocities against the ocean velocity at the first vertical level below the sea ice in the LTC model (0.6 m). When Ri_{bulk} exceeded a critical value (Ri_c) of 0.65 (Price et al., 1986), deepening due to turbulent mixing was assumed to terminate. Thus, the depth of the active mixing layer for this study was considered depths shallower than $Ri_{bulk} = 0.65$.

3.2 Boundary conditions

The LTC model is forced by momentum, heat, and mass (salt) boundary conditions through an ice-ocean interface submodel. Full descriptions of these boundary conditions are provided in the subsections below along with the methods and observations that were used to drive them.

3.2.1 Interface stresses

Ice-ocean interface stresses (τ_o) were calculated from ice speeds driven by observed 2-m winds and scaled by the appropriate air-ice and ice-ocean drag coefficients. The air-ice drag coefficient was calculated by

$$C_{d(2m)} = \frac{u^2_{*(2m)}}{U^2_{(2m)}}, \tag{8}$$

where $u_{*(2m)}$ is the friction velocity computed from the AOFB 29 sonic anemometer wind stresses and U is the mean wind at 2 m relative to the sea ice. For this study, a 30-day average (YDs 224–253) $C_{d(2m)}$ of 3.4 × 10^{-3} was used. Under-ice drag within the LTC ocean surface layer is controlled by the roughness length constant (z_o), which is a measure of the length scale of the under-ice roughness elements. Roughness length was calculated by

$$z_o = he^{-k/\sqrt{C_{d(h)}}}, \tag{9}$$

where κ is the Von Karman's constant (0.4) and h is the distance from the interface (McPhee, 2002). Similar to the air-ice C_d, a 30-day average (YDs 226–255) ice-ocean $C_{d(4.5m)}$ of 6.3 × 10^{-3} was estimated from the flux package onboard AOFB 29 which resulted in an average z_o value of 0.029 m.

3.2.2 Interface submodel

The LTC submodel calculates the kinematic heat and salt balances at the ice-ocean interface to estimate the amount of melting or freezing that occurs at the ice base and supplies the resulting freshwater/salt to the ocean boundary layer. The submodel kinematic heat balance is calculated by

$$-\dot{q} + <w'T'>_o = w_o Q_L, \tag{10}$$

where $\dot{q}$ is the kinematic sea ice conductive flux and $<w'T'>_o$ is the interface kinematic ocean-to-ice heat flux (McPhee, 2008). The imbalance of these two terms yields the kinematic latent heat flux ($w_o Q_L$) which determines the basal melt/freeze rate. The w_o term is the interface velocity (melt rate) and Q_L is latent heat term corrected for sea ice salinity (Maykut, 1985). The LTC model uses the following relation to calculate sea ice conductive flux,

$$\dot{q} = \frac{-K_{ice}\dfrac{dT}{dz}}{\rho_{sw} c_p}, \tag{11}$$

where dT/dz is the vertical thermal gradient in the sea ice and K_{ice} is the thermal conductivity of sea ice using the approximation of Untersteiner (1961) (~ 2 J m^{-1} K^{-1} s^{-1}). For this study, the in-ice temperature string data onboard AOFB 29 was linearly interpolated to the 15-min time steps of the LTC model to represent dT/dz in Equation 11.

The submodel kinematic salt balance is calculated by

$$<w'S'>_o + w\left(S_{ice} - S_o\right) = 0, \tag{12}$$

where $<w'S'>_o$ is the oceanic turbulent salt flux, S_{ice} is the sea ice salinity, and S_o is the interface salinity. The sum of the basal melt rate (w_o) and the rate of meltwater drainage through the sea ice (w_p) represent the total interface velocity ($w = w_o + w_p$). For this study, we generalized w_p to represent all freshwater sources other than basal melt (lateral melt and/or drained surface sea ice melt) by,

$$w_p = w_{fwc} - w_o, \tag{13}$$

where w_{fwc} is the total upper ocean freshwater storage (*FWC*) calculated from Equation 3 divided by the CTD cast time interval (*FWC/Δt*), and w_o is the basal melt rate/velocity predicted by the LTC model.

3.3 Initial conditions

Upper ocean initial conditions were specified by 0.25-m binned salinity and temperature CTD data that were linearly interpolated to the 100 vertical levels in the LTC model domain between 0 and 60 m (0.6-m resolution). Sea ice thickness was set to 2 m based on the average values of the ice surveys conducted around the study site ice floe (not shown). Ice type in the vicinity of the Ice Camp was a mixture of first-year and multi-year ice, therefore a bulk sea ice salinity of 4 was used in the LTC submodel (Vancoppenolle et al., 2006).

The LTC also allows for distributed absorption of incoming solar radiation over the water column (Q^H), which is calculated with the extinction relation

$$Q^H = \frac{f_{sw} F_{rad}}{z_{sw}} e^{\frac{z}{z_{sw}}}, \tag{14}$$

where f_{sw} is the fraction of solar radiation that penetrates the sea ice, F_{rad} is the incident solar radiative fluxes from the AWS 5 and AOFB 29 pyranometers, z is the depth of the water beneath the ice base, and z_{sw} is the e-folding depth equal to 4 m (McPhee, 2008). Providing a good estimate of f_{sw} is critical to the LTC model mixed layer heat balance. Therefore, we followed the methods of Gallaher et al. (2016) to threshold visible satellite imagery pixel values and estimate the through-open-water and through-ice solar radiative fluxes to the ocean. Results of the visible imagery mask (**Figure 5**) estimated open water fraction at 0.07, melt pond fraction at 0.23; and the area of bare ice at 0.7. Thus,

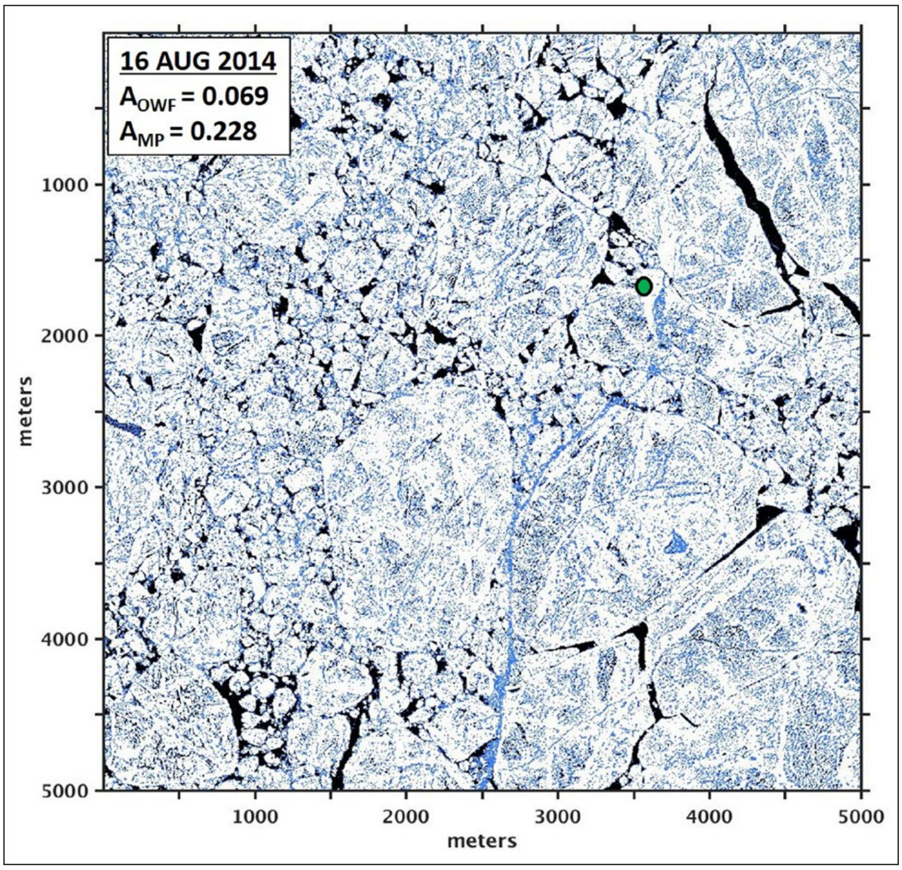

Figure 5: Surface sea ice conditions at MIZ Cluster 5. Masked high-resolution (1-m) visible satellite image showing open water (A_{OWF}, false color black), melt ponds (A_{MP}, false color light blue), and bare sea ice (white). The areal coverages of open water, melt ponds, and sea ice were used to estimate the fraction of radiative fluxes penetrating the sea ice (f_{sw}) for use in the LTC model. The location of MIZ cluster 5 is indicated by the green dot. DOI: https://doi.org/10.1525/elementa.195.f5

the average f_{sw}, or transmittance, of short-wave radiation to the ocean over the 4-day Ice Camp was estimated at 0.12.

4. Results

4.1 Ice camp observations

In general, winds were light during the MIZ-KOPRI Ice Camp. Mostly clear skies resulted in downwelled shortwave radiative fluxes approaching 400 W m^{-2} (**Figure 4a**). At the start of the time series (YD 221.8), the surface boundary layer was well mixed and extended to a depth of ~ 20 m (**Figure 4b–c**). This surface mixed layer was underlain by the early summer halocline and NSTM, around 23-m depth, with no evidence of a shallower NSTM feature. A moderate, 6 m s^{-1}, wind event occured on YD 223.4 and generated surface mixing that added ~ 6 cm of freshwater to the ocean volume above the 1022 kg m^{-3} isopycnal (**Figure 4d**).

Upper ocean properties changed after the YD 223.4 mixing event. Starting on YD 223.7, the upper 20 m of the ocean warmed. At YD 224.0, the late summer NSTM criteria ($\delta T > 0.17°C$) was met briefly (**Figure 4c**, red dot). At the same time, surface-ocean stratification (represented by the squared Brunt-Väisälä frequency, N^2) increased and the occurrence of the near-surface N^2 maxima (**Figure 4b**, yellow dots) indicates that the late summer halocline developed at a depth of about 15 m. During the final two days of the time series, freshwater storage gradually increased (**Figure 4d**) and the late summer halocline strengthened. At YD 224.6, a temperature maximum appeared between depths of 10 and 15 m (**Figure 4c**), marking the formation of the late summer NSTM. The late summer NSTM maintained an average depth of ~ 12 m through the end of the time series, making the NSTM layer the control volume between 7 and 17 m (**Figure 4c**, black dashed lines). Heat storage calculations within this control volume (**Figure 4d**) show that the NSTM layer accumulated ~ 1.1 MJ m^{-2} of heat by YD 225, before undergoing heat loss toward the end of study period. Observations from the Ice-Tethered Profiler 80 (ITP 80), deployed ~ 200 m from R/V *Araon* on YD 226, indicate the late summer NSTM survived for another 10 days under the C5 ice floe (not shown), but was then mixed out by strong winds in late August. Although the late summer NSTM was weak compared to the early summer NSTM, the signal was distinctive and similar to the early summer NSTM. In the following results subsections, we present the use of these high-resolution observations and LTC model output to identify mechanisms that led to NSTM development at the C5 site. The analysis was then extended to a modeling study of the early summer NSTM at MIZ C2, to gain an overall understanding of NSTM formation processes.

4.2 LTC model representation

To validate the LTC model and model inputs, we tested if the model could reasonably represent the upper ocean conditions observed during the MIZ-KOPRI Ice Camp. Employing the methods outlined in Section 3, we ran the LTC model in two freshwater input modes. In mode

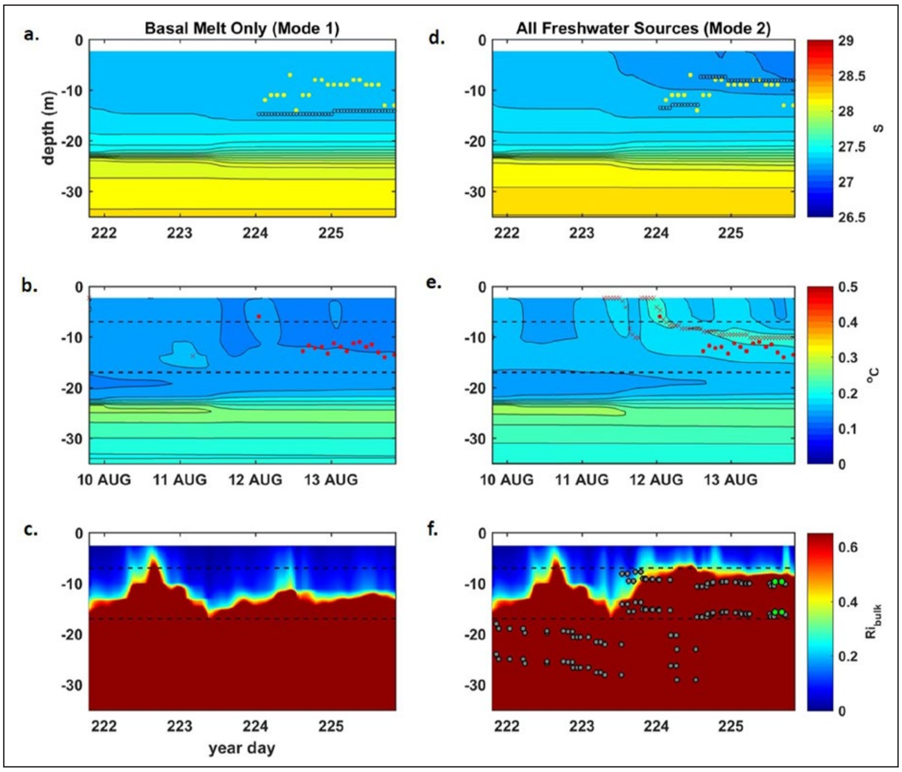

Figure 6: LTC model reproduction of the late summer NSTM at MIZ Cluster 5. LTC model results of the late summer halocline and NSTM for **(a–c)** basal melt only ($w_p = 0$) and **(d–f)** for all freshwater inputs (basal melt + w_p) as observed at the MIZ-KOPRI Ice Camp. Panels **(a)** and **(d)** are salinity (S) with modeled (black circles) and observed (yellow dots) near-surface N^2 maxima. Panels **(b)** and **(e)** are temperature above freezing with modeled (red Xs) and observed (red dots) NSTM. Panels **(c)** and **(f)** are the bulk Richardson number (Ri_{bulk}) estimates of the upper ocean using Equation 7. NSTM layer is indicated by horizontal black lines. Gray dots on Figure 6f are the deployment depths of the NPS Turbulence Frame during the Ice Camp with the green dots framing the period of the YD 225.65 case study. DOI: https://doi.org/10.1525/elementa.195.f6

one (**Figure 6a–c**), only the model-derived basal melt rate (w_o) was included as a freshwater source to the ocean boundary layer (w_p = 0). Salinity and δT outputs (**Figure 6a–b**) indicate that freshwater from basal melt alone could not reproduce the late summer NSTM and halocline. Evaluation of the bulk Richardson number (Ri_{bulk}, **Figure 6c**) shows that turbulent penetration was shallow; however, during the final two days of the simulation, the active mixing layer extended about half way through the NSTM layer and mixed the absorbed solar heat input.

For mode two (**Figure 6d–f**), freshwater from all sources was included in the boundary conditions ($w_o + w_p$). Salinity and δT outputs for this simulation (**Figure 6d–e**) yield a realistic depiction of the observed late summer NSTM and halocline. Additionally, the model NSTM (red Xs) and N^2 maxima (black circles) share similar depths to the observed NSTM (red dots) and N^2 maxima (yellow dots). Ri_{bulk} calculations (**Figure 6f**) show similar conditions to mode one out to the YD 223.4 wind event; however, during the final two days of the simulation, the depth of turbulent penetration was limited to depths above the NSTM layer. These results suggest that the late summer NSTM was developed by local processes and that this temperature maximum was not the result of lateral advections of heat into the study site. The excellent reproduction of the late summer NSTM using the observed freshwater inputs (mode two) also provides confidence that the processes responsible for development of the NSTM were captured in the one-dimensional LTC model physics and that the imposed initial and surface boundary conditions were accurate.

4.3 LTC model fluxes

To further elucidate boundary layer processes affecting the evolution of the late summer NSTM, we examined fluxes of radiation, momentum, heat, and buoyancy in the LTC. The exponential decay of visible light energy with depth limited the magnitude of radiative fluxes reaching the NSTM layer. Absorbed solar heat fluxes averaged only ~ 0.6 W m^{-2} m^{-1} in the 7–17 m volume (**Figure 7a**) resulting in an integrated NSTM layer total flux of ~ 6 W m^{-2}. This rate of heating yielded a total radiative heat input of 2.1 MJ m^{-2} to the late summer NSTM layer over the 4-day ice camp; however, not all this heat was retained in the NSTM layer during the first two days of the time series (**Figure 4d**). Model output of eddy viscosity (K_m) (**Figure 7b**) and Ri_{bulk} (**Figure 6f**) show that moderate turbulent mixing occurred in the NSTM layer during the YD 222 and 223.4 wind events. These periods of active turbulence transported heat upwards and out of the late summer NSTM layer.

Large buoyancy fluxes were also observed with the YD 223.4 mixing event (**Figure 7d**). These fluxes were elevated during this event for two reasons: 1) the mix down of freshwater added by the w_p term in the LTC submodel (based on freshwater storage observations); and 2) the turbulent transport of salt upward from the early summer halocline. These two processes resulted in tightening of the isohalines between 10 and 20 m and likely contributed

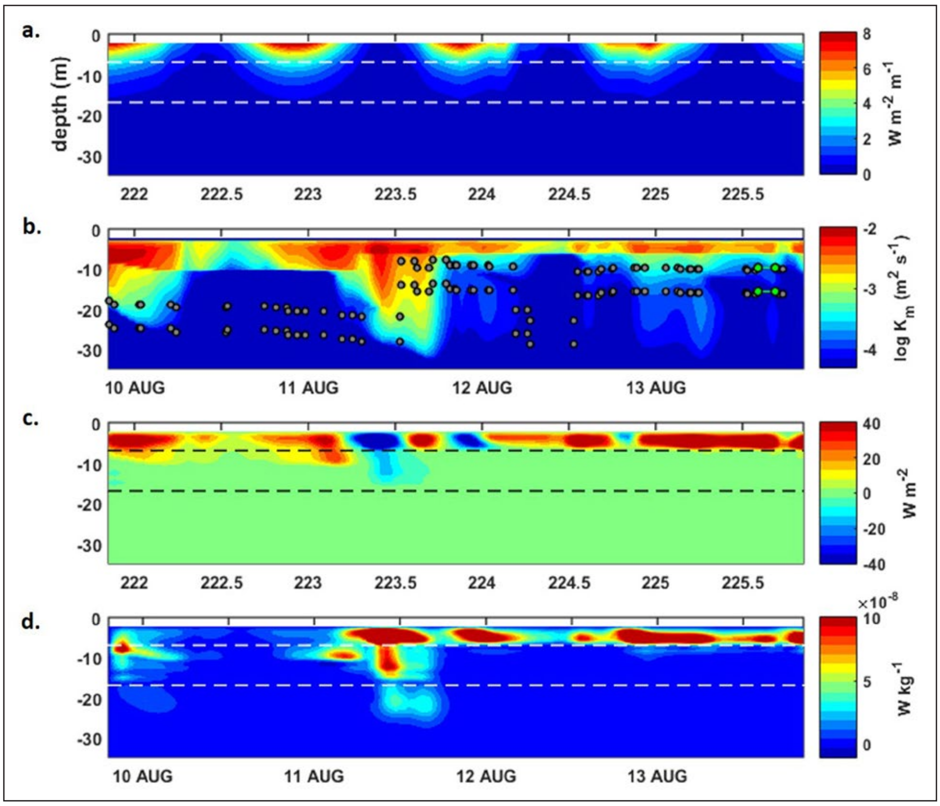

Figure 7: LTC model radiative and turbulent fluxes at MIZ Cluster 5. LTC model output from the MIZ-KOPRI Ice Camp showing the **(a)** upper ocean absorbed solar radiative flux, **(b)** eddy viscosity (K_m), **(c)** dynamic heat flux, and **(d)** buoyancy flux. The horizontal white and black dashed lines on the panels denote the NSTM layer. Gray dots on Figure 7b indicate the deployment depths of the NPS Turbulence Frame with the green dots framing the period of the YD 225.65 case study. DOI: https://doi.org/10.1525/elementa.195.f7

to the formation of the late summer halocline. This finding was based on the observations of the near-surface N^2 maxima which appeared in the model and the observations around 15-m depth (**Figures 6d** and **4b**).

The late summer NSTM layer began to warm immediately after the YD 223.4 mixing event, in both the observations (**Figure 4c–d**) and the LTC model (**Figure 6e**). To assess the relative significance of radiative and turbulent fluxes on the evolution of the late summer NSTM over the last two days of the time series, we present time-averaged depth profiles of turbulent heat flux convergence (dF_H/dz), turbulent buoyancy flux convergence ($d\langle w'b'\rangle/dz$), and radiative flux convergence ($dF_{rad\text{-}ocn}/dz$) in **Figures 8a–b**. The peak in turbulent heat and buoyancy flux convergence occurred at ~ 6 m and was above the late summer NSTM layer (**Figure 8a–b**). Time integration of the turbulent heat fluxes in the 7–17 m layer (**Figure 8c**, black line) suggests that these fluxes did not contribute to NSTM layer heating. However, the convergence of turbulent buoyancy fluxes had a significant influence on increasing stratification near the top of the NSTM layer. This increase in stratification can be seen in the model N^2 values (**Figure 8d**) which show an intensifying peak around 8-m depth. The displacement of this N^2 peak below the buoyancy flux peak is likely associated with the stronger turbulent mixing present at the base of the active mixing layer (**Figure 7b**). The N^2 peak marks the development of the late summer halocline which occurs just above the developing late summer NSTM (red Xs). The observed N^2 values (contours for values $> 3 \times 10^{-3}$ s^{-2}) and NSTM (red dots) are also plotted on **Figure 8d** and show similar depths and orientation to the model features. Development of the summer halocline is a key event for the development of NSTM as it prevents significant turbulence from penetrating into the NSTM layer (**Figures 6f** and **7b**).

About two-thirds of the solar radiative flux was absorbed in the top 7 m of the water column (**Figure 7a**); however, heat storage in this layer was small (**Figure 4c**), because this heat was readily transported to the ice base where it caused melting (**Figure 7c**). In the NSTM layer, absorbed solar radiation was considerably less, but as previously

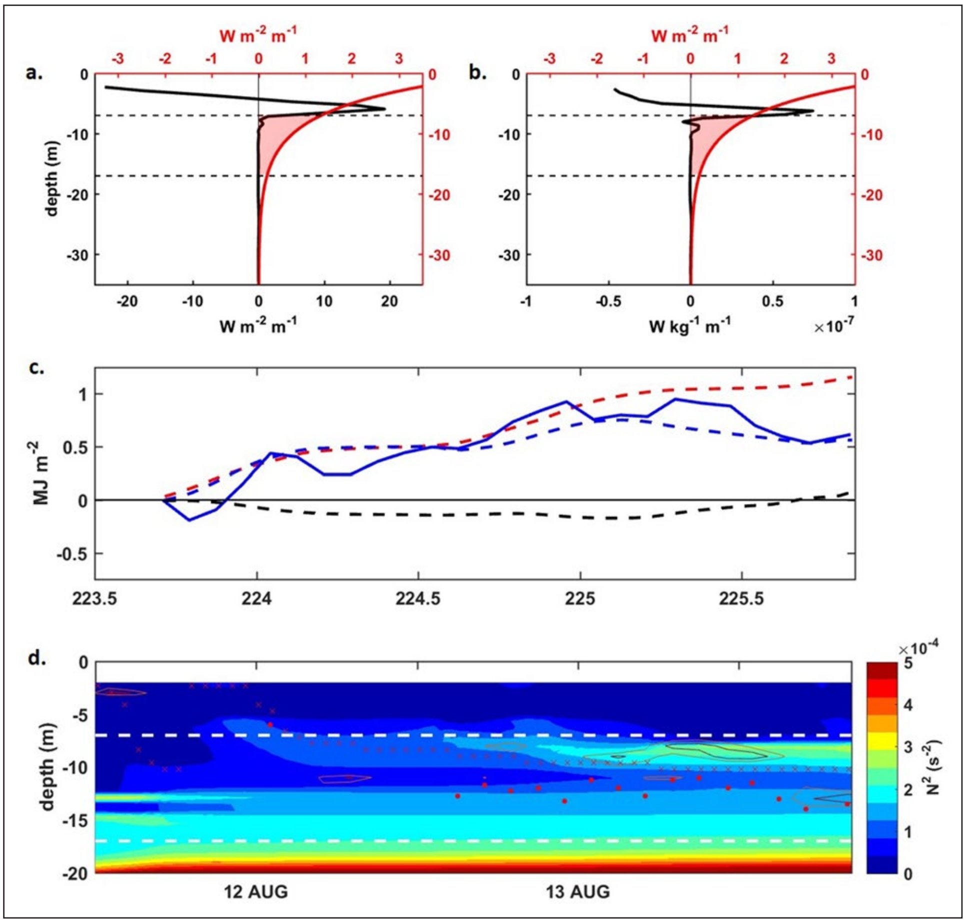

Figure 8: Radiative and turbulent vertical flux convergence of the late summer NSTM. LTC model output of the **(a)** dynamic heat flux convergence (black line), **(b)** buoyancy flux convergence (black line), and (b–c) radiative flux convergence (red line) averaged between YDs 223.7 to 225.8. Red-shaded areas show absorbed radiative flux overlapping the NSTM layer. **(c)** Model output displaying the cumulative NSTM layer heat storage (blue dashed line), integrated absorbed radiative fluxes (red dashed line), and integrated dynamic heat fluxes (black dashed line) with the observed NSTM layer cumulative heat storage (solid blue line). **(d)** Plot of the LTC model N^2 (colorfill) and observed N^2 (contours $> 4 \times 10^{-4}$ s^{-2}) showing the relative depths of the summer halocline to the modeled (red Xs) and observed (red dots) NSTM. DOI: https://doi.org/10.1525/elementa.195.f8

discussed, buoyancy fluxes near the top of the NSTM layer substantially inhibited turbulence penetration below 7-m depth (**Figure 7b**). As a result, model (**Figure 8c**, blue dashed line) and observed (blue solid line) heat storage increased in the late summer NSTM layer. Integration of absorbed radiative heat fluxes in the NSTM layer (**Figure 8c**, red dashed line) indicates that sufficient solar heat was available to support development of the NSTM. After YD 225, model and observed NSTM heat storage decreased due to a slight increase in mixing (**Figure 7b**), which entrained heat from the upper portions of the layer (**Figures 4c** and **6e**). These results show that the source of heat to the developing late summer NSTM during the last two days of the time series was solar radiative flux absorbed within the NSTM layer. Additionally, increases to buoyancy above (**Figure 8b**) and within the NSTM layer (**Figure 7d**) aided the retention of this heat by inhibiting turbulent mixing.

4.4 Wind and buoyancy sensitivity testing

Results from the previous section show that the NSTM develops from an interplay between wind-driven mixing, buoyancy forcing, and proximity to shortwave radiative heating. We next investigated the influence of these processes on NSTM development by systematically varying LTC inputs for wind and freshwater. We start this section by presenting four case studies as examples of this investigation.

In Case I, winds were increased 25% from observed and freshwater input was kept at the observed level of 0.1 m. The increased wind forcing completely mixes away the late summer NSTM in the model (**Figure 9a**). In Case II, winds were increased 50% and freshwater input was doubled to 0.2 m. Some warming of the NSTM layer occurs (**Figure 9b**); however, the signal is reduced and it occurs deeper than the observed NSTM. These results indicate that the large increase in freshwater established a pycnocline to protect the NSTM from mixing; however, the stronger winds deepened the protective pycnocline further from the radiative source resulting in smaller heat storage. In Case III, winds were reduced 25% and freshwater input was as observed. The NSTM develops near the top of the 7–17 m control volume (**Figure 9c**) and the peak temperature is higher than the observed NSTM. These results suggest that the turbulent boundary layer shoaled in response to the weaker wind forcing, moving the summer halocline closer to the radiative source. In Case IV, winds remained unchanged and freshwater was reduced 25%. The late summer NSTM develops at nearly the same depth and timing as the control run and the observations, but at a lower temperature (**Figure 9d**), which indicates that the weaker summer halocline was less able to prevent turbulent mixing from entraining heat out of the NSTM layer.

The sensitivity study was then expanded to 24 different combinations of wind and freshwater input to determine which of these forcings more heavily controlled development of the late summer NSTM. **Figure 10** shows the cumulative heat storage gain in the 7–17 m control volume across the time series for each of these 24 cases, which tested scenarios of wind and freshwater content between ± 50% of the observed values. Results show that the mean difference in heat storage between the 150% and 50% wind categories equaled +2.03 MJ m^{-2}, which indicates that changes in wind forcing greatly affected the amount of heat storage accumulated in the model NSTM layer. The mean differences in heat storage between the 50% and 150% freshwater content categories yielded +1.18 MJ m^{-2}, which was 42% less than the LTC model wind response. These results show that, under this range

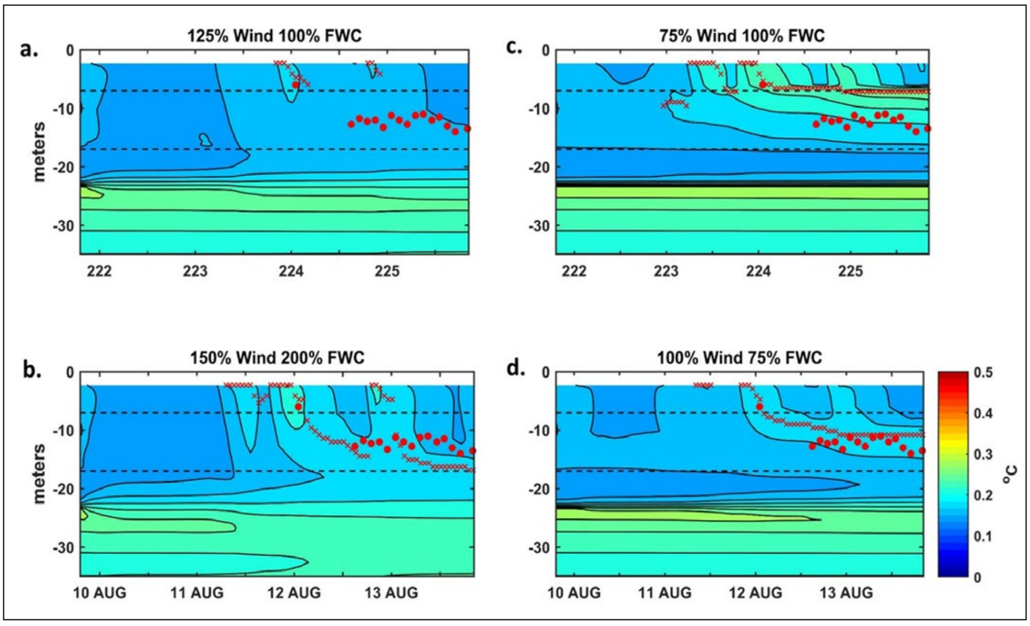

Figure 9: LTC model NSTM wind and buoyancy sensitivity tests. (a–d) LTC model output of the temperature above freezing for the wind and buoyancy sensitivity test cases. Modeled (red Xs) and observed (red dots) NSTM depths are annotated on each plot. Test case modifications to observed winds and freshwater input (FWC) are indicated above each plot. DOI: https://doi.org/10.1525/elementa.195.f9

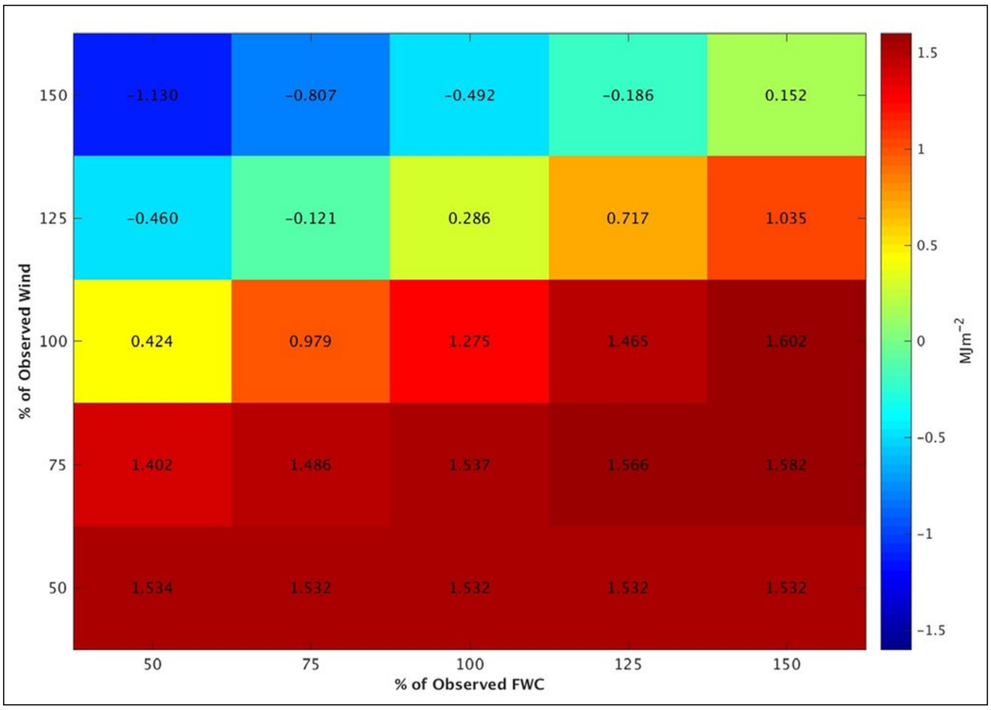

Figure 10: LTC model NSTM heat storage wind and buoyancy sensitivity tests. LTC model results of the 25 different wind and buoyancy test scenarios conducted on the late summer NSTM. Numbers in the matrix indicate the cumulative heat storage gain/loss in the NSTM layer (7–17 m) across the time series (YDs 221.8–225.8). DOI: https://doi.org/10.1525/elementa.195.f10

of model conditions, development of the late summer NSTM was controlled primarily by the character of the wind forcing.

4.5 Evolution of turbulent eddies through the NSTM layer

For the NSTM to survive, sufficient stratification must be established near the top of the NSTM layer to prevent subsequent mixing events from transporting heat out of the layer. The lack of turbulence observed in the NSTM layer from the Turbulence Frame and the high Ri_{bulk} values predicted by the LTC model at the Frame deployment depths (**Figure 6f**, gray dots) are consistent with this understanding. However, low-level turbulence was observed by the Turbulence Frame in the NSTM layer around YD 225.65 (see **Figures 6f** and **7b** for time/depth reference, green dots). This event is investigated in the analysis below to understand how turbulent eddies behave in weak summer halocline stratification.

To study the evolution of turbulent eddies within, and near, the late summer halocline and NSTM, we analyzed vertical velocity spectra from the Turbulence Frame flux packages. McPhee and Martinson (1994) show that the turbulent energy peak found in the vertical velocity spectrum scaled by the wavenumber ($kS_{ww}(k)$) can be used to find the peak mixing length (λ) in the ocean boundary layer by

$$\lambda_{peak} = \frac{0.85}{k_{\max}}, \tag{15}$$

where k_{max} is the wavenumber associated with the turbulent peak. Conversion of the frequency-space spectrum to a wavenumber-space spectrum was accomplished by using the Taylor frozen field hypothesis (Taylor, 1938). In the $kS_{ww}(k)$ spectrum, the k multiplier changes the –5/3 power law expected of the inertial subrange (Kolmogorov, 1941) to –2/3. Using a scaling of the S_{ww} spectrum within the inertial subrange, turbulent kinetic energy (TKE) dissipation (ε) can be found using the inertial-dissipation method (Hinze, 1975; McPhee, 1994)

$$\varepsilon = \left[\frac{3}{4\alpha_{\varepsilon}} S_{ww}(k) k^{\frac{5}{3}}\right]^{\frac{3}{2}}, \tag{16}$$

where α_{ε} is the Kolmogorov constant (0.51), $S_{ww}(k)$ is the vertical velocity power spectrum, and k is the wave number.

The presence of a well-developed inertial subrange in the Turbulence Frame measurements for the 40-min period around YD 225.65 (**Figure 11**) confirms the existence of fully developed turbulence at the 9-m (blue) and 15-m (green) sensor depths. For comparison, a turbulent spectrum from a high wind event (~ 10 m s^{-1}, magenta) at AOFB 29 on YD 251 is plotted, demonstrating how weak the turbulence was within the late summer halocline and NSTM layer. The turbulent energy peaks from the Turbulence Frame autospectra were 1–2 decades lower than the high wind case. Turbulent mixing in the NSTM layer was able to penetrate despite the presence of the late summer halocline because density gradients were very weak ($d\rho/dz \sim 0.02$ kg m^{-3} m^{-1}) when compared to the early summer halocline ($d\rho/dz \sim 0.2$ kg

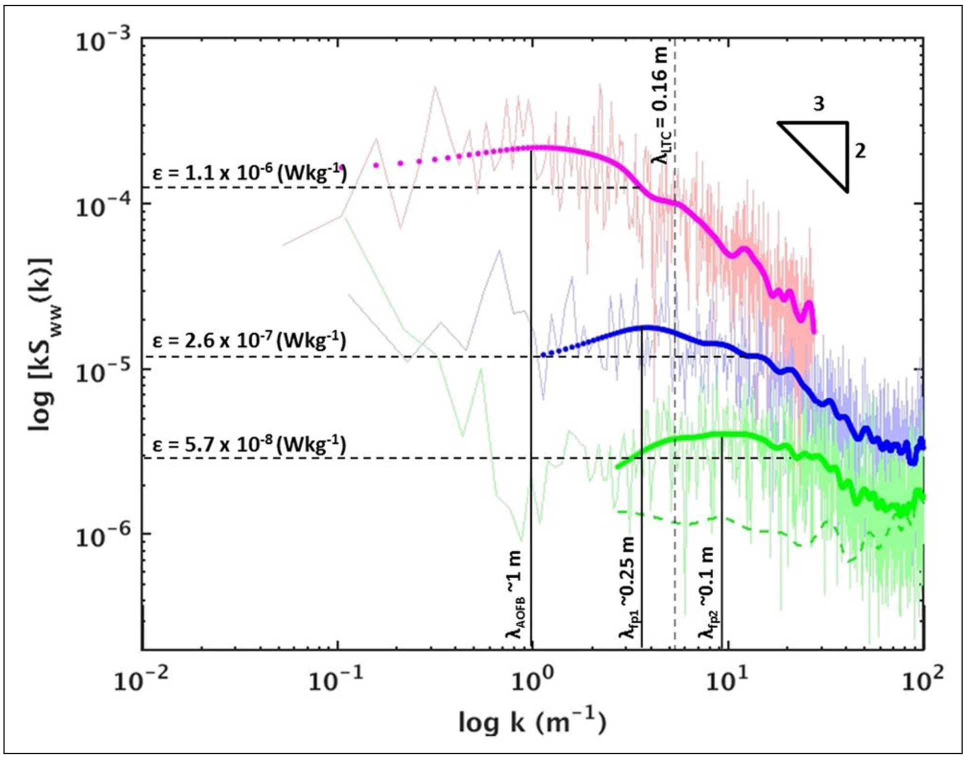

Figure 11: Observed turbulent spectra in the late summer halocline and NSTM. Power spectra of wavenumber-scaled vertical velocity for the high wind case at AOFB 29 (magenta), upper Flux Frame package at 9-m depth (blue), and lower Flux Frame package at 15-m depth (green). In this k-scaled spectrum, the k multiplier changes the −5/3 power law expected of the inertial subrange (Kolmogorov, 1941) to −2/3. Convolution filter results (solid color lines) highlight the turbulent energy peaks for each spectrum and the corresponding wavenumbers (k_{max}, black vertical lines) by which estimates of mixing length (λ) were calculated using Equation 15. Corresponding LTC model λ is indicated by the vertical dashed line. Estimates of turbulent kinetic energy (TKE) dissipation (ε) were made for each spectrum using the inertial-dissipation method (Equation 16) to characterize turbulent eddy intensity in the NSTM layer DOI: https://doi.org/10.1525/elementa.195.f11

$m^{-3}\ m^{-1}$). For comparison, the 1-hr average Richardson number across the Turbulence Frame around YD 225.65 was ~ 0.5; however, application of the same shear values to the early summer density gradients yields an average Ri of ~ 8.

Estimations of the turbulent mixing length (λ) from Equation 15 show that λ contracted from ~ 25 cm near the top (9 m) of the NSTM layer to ~ 10 cm near the bottom (15 m) (**Figure 11**). These values are similar to the model-predicted λ_{LTC} of 16 cm for both levels. Estimated TKE dissipation (ε) using Equation 16 showed that ε_{fp1} values were 4 times ε_{fp2}, but that the dissipation rate for the upper flux package was 1/4 that of ε for the strong wind case estimated at the 2.5 m level (**Figure 11**, magenta line). Analysis of turbulent spectra adjacent in time to this event (**Figure 11**, green dashed line) indicate that for most of the period when the NSTM was present, turbulence levels were below the very low noise floor of the acoustic travel-time velocimeters. These results suggest that, despite the presence of weak turbulence, transport rates were too small to remove significant amounts of heat from the NSTM layer.

4.6 Comparing the early and late summer NSTMs

The analysis of the MIZ-KOPRI Ice Camp conditions at MIZ C5 reveal that the late summer NSTM develops under a delicate balance of weak wind-forced ice-ocean interface stresses and modest buoyancy fluxes, but how does this balance differ for the early summer NSTM? To examine this science question we modeled the formation of the early summer NSTM at MIZ Cluster 2 (C2) and next compare these results to the late summer NSTM case.

4.6.1 LTC model initial and boundary conditions at MIZ Cluster 2 (C2)

To successfully compare the early and late summer NSTM cases, the LTC model must be able to reasonably reproduce the observed conditions at MIZ C2 in early summer. Similar to MIZ C5, the observations made at MIZ C2 were extensive and provided an excellent characterization of the ice-ocean system in order to properly initialize the LTC model and update the boundary conditions. For the initial conditions, we used the upper ocean salinity and temperature observations from AOFB 33 at 4.5 m merged with observations from ITP 77 made between 6 and 60 m. For the boundary conditions, observations of air-ice wind stress were not made at MIZ C2, therefore the LTC model was driven by ice speeds obtained from differencing 5-min

GPS positions at AOFB 33. Sea ice temperature gradients were provided by the 16-element temperature string on AOFB 33. The sea ice percolation velocity (w_p) was set to zero except on YD 189 when the equivalent of 0.25 m of freshwater was introduced based on the melt pond drainage estimates made by Gallaher et al. (2016). The LTC model was updated with the MIZ C2 underice drag coefficient of 2.6 x 10^{-3} ($Cd_{(4.5m)}$) based on measurements made by the turbulence package on AOFB 33. For shortwave radiative input (Q^H), we set the fractional solar radiation terms in Equation 14 ($fsw{\cdot}Frad$) to the ocean radiative fluxes estimated by Gallaher et al. (2016) at MIZ C2. All other model parameters, constants, and setups remained as outlined in Section 3. The model simulation period began after the mixing event on YD 184 and ended on YD 198.

4.6.2 LTC model representation of the early summer NSTM at MIZ C2

The LTC model run for the early season case reasonably reproduces the observed conditions. The observed early summer halocline (**Figure 12a**, yellow dots) matched well with the depth of the modeled near-surface N^2 maximum (**Figure 13a**). Likewise, the depth of the observed NSTM (**Figure 12b**, red dots), based on the criteria of Jackson et al. (2010), was reasonably close to the depth of LTC temperature maximum, with only minor deviations between YDs 194 and 196 (**Figure 13b**). These model results corroborate the assertions of Gallaher et al. (2016) that melt pond drainage in early July 2014 led to the development of the summer mixed layer, summer halocline, and associated NSTM. To compare the relative influences of ice motion and meltwater input on development of the early summer halocline and NSTM, we decomposed the bulk Richardson number (Equation 7) into its shear (ΔV^2) and buoyancy ($\Delta b = g\Delta\rho/\rho_{sw}$) components. These components were evaluated from the LTC model across the summer mixed layer (Δh) defined from the model surface (0.6 m) to the summer haolcline depth (near-surface N^2 maximum). As expected, the buoyancy component (**Figure 13c**) increased substantially (0.004 m s^{-2}) on YD 189; however, a corresponding increase in the Ri_{bulk} did not immediately occur (**Figure 13e**) due to the very shallow surface mixed layer (small Δh) following the simulated melt pond drainage event. After the early period increase, Δb values decreased to just below the model period average of 0.0022 m s^{-2} (**Figure 13c**, blue dashed line) and were well above the late summer modeling study mean (**Figure 13c**, red dashed line). These increases in upper ocean buoyancy led to a high Ri_{bulk} condition throughout the early summer case with average Ri_{bulk} values nearly three times that of the late summer case, at 11.5 and 4.3, respectively (**Figure 13e**). This finding indicates that stratification within the early summer halocline greatly inhibited turbulent mixing despite the slightly higher average ΔV^2 component (**Figure 13d**). These results suggest that the early summer halocline and associated NSTM are dominated by buoyancy forcing in contrast to the wind sensitive late summer case.

4.6.3 LTC model comparisons of the early and late summer NSTM under MIZ C5 conditions

The LTC model results and observations from MIZ C2 and C5 suggest that the differences between the early and late summer NSTMs were the result of variations in interfacial freshwater input from sources other than

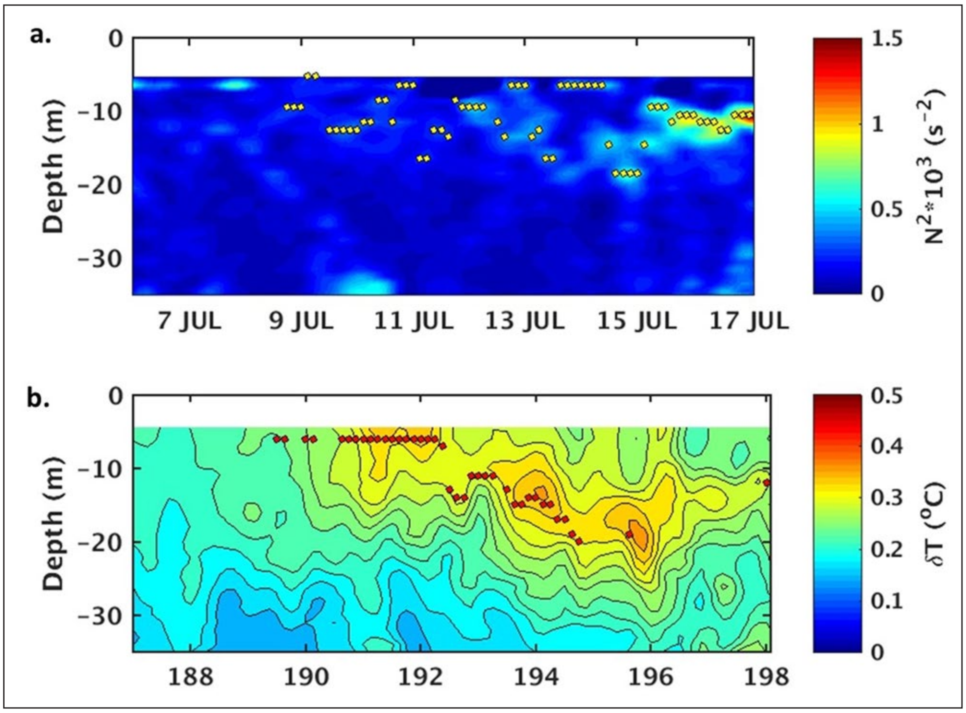

Figure 12: Early summer NSTM observations at MIZ Cluster 2. Cluster 2 observations of **(a)** N^2 with the summer halocline depths (yellow dots) and **(b)** temperature above freezing with observed NSTM depths (red dots) following the criteria of Jackson et al. (2010). DOI: https://doi.org/10.1525/elementa.195.f12

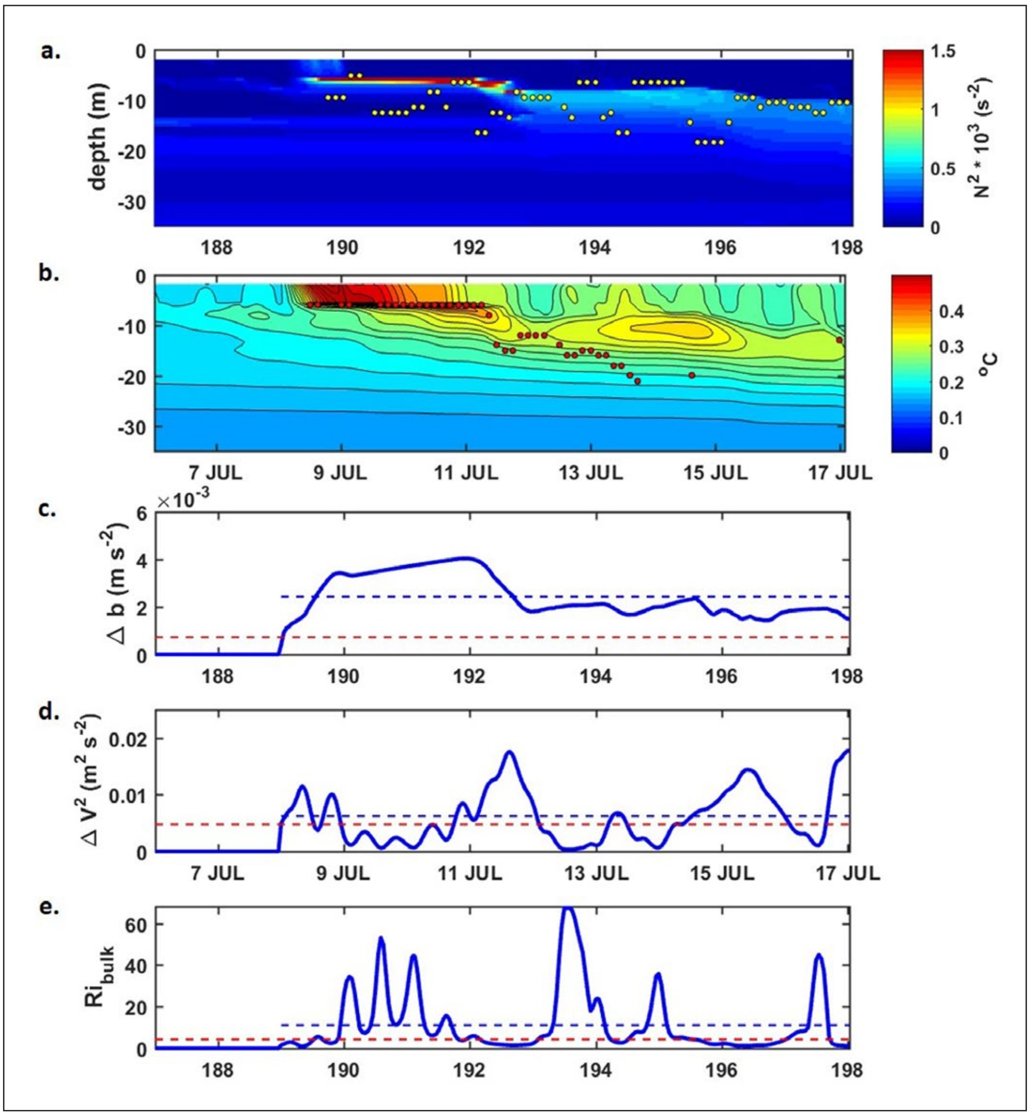

Figure 13: LTC model simulations of the early summer NSTM at MIZ Cluster 2. Plotted are the **(a)** modeled N^2 with observed summer halocline depths (yellow dots) and **(b)** modeled temperature above freezing with observed NSTM depths (red dots, criteria of Jackson et al., 2010). In this case, 0.25 m of freshwater was added to the model on YD 189 to simulate the observed melt pond drainage. **(c)** Corresponding model buoyancy (Δb) and **(d)** shear (ΔV^2) components of the **(e)** bulk Richardson number (Ri_{bulk}) are presented along with mean values (blue dashed lines) for each. For comparison, the mean values of the Ri_{bulk} parameters from the late summer case at MIZ C5 are also provided (red dashed lines). Evaluation of the Ri_{bulk} and its components began after the melt pond drainage event. DOI: https://doi.org/10.1525/elementa.195.f13

basal ice melt. To ensure that differences in time of year (solar input and basal melt rate), ice conditions (ice roughness/drag and concentration), or location in the Canada Basin (wind forcing) did not affect the conclusions made thus far, we imposed the early summer melt pond drainage event on the model settings and boundary conditions used at MIZ C5. This step allows for a direct comparison of the early and late summer NSTM under identical surface forcing conditions. As with the MIZ C2 case, the percolation velocity (w_p) was setup to deliver 0.25 m of freshwater to the ocean boundary layer over a one day period (YD 223 for this case). Results show that a distinctive near-surface N^2 maximum and temperature maximum appear in the model (**Figure 14a–b**) following the release of the simulated melt pond water. Inspection of the early (**Figure 14a–b**) and late (**Figure 14c–d**) summer cases side-by-side show that the NSTM is ~ 50% warmer (0.3°C verses 0.2°C) at the early summer site and was supported by a stronger halocline. In **Figure 14c** and **f**, the Ri_{bulk} critical value (R_c = 0.65) and the next three multiples of the critical value (i.e., $2Ri_c$, $3Ri_c$, and $4Ri_c$) are plotted to compare the vertical distribution of the halocline stratification. In the early summer case, the vertical gradient is tight, indicating a high Ri_{bulk} condition in the upper early summer halocline. Conversely, the late summer contour gradient is relaxed, suggesting moderate increases in stress could easily overcome the late summer halocline stratification. As observed during the C2 case, evaluation of the early summer Δb and Ri_{bulk} values are consistently greater than the late summer case (**Figure 15a** and **c**). More importantly, the depth of the

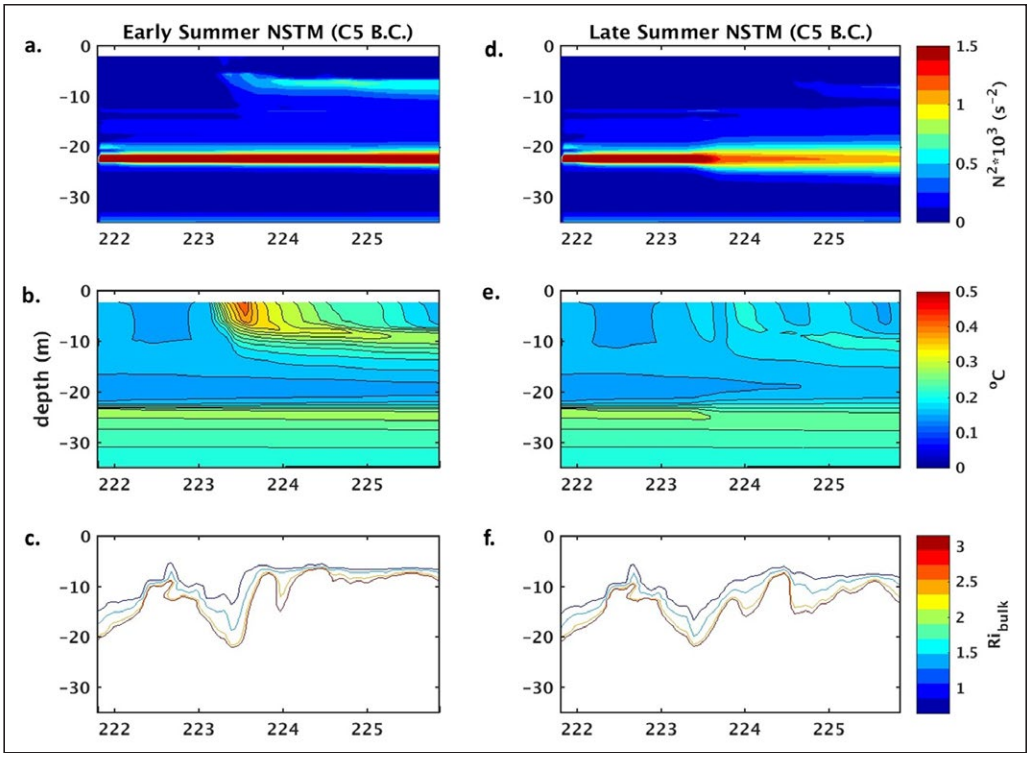

Figure 14: Comparisons of the early and late summer NSTM using MIZ C5 surface forcing. LTC model output of the **(a)** N^2, **(b)** departure from freezing, and **(c)** contours of Ri_{bulk} (0.65, 1.3, 1.95, 2.6) for the early summer case using MIZ C5 air-ice-ocean conditions. For this case, 0.25 m of freshwater was added to the model on YD 223. **(d, e, f)** Same format as the left-hand panels but for the late summer case using observed freshwater input (0.1 m) during the MIZ-KOPRI Ice Camp. DOI: https://doi.org/10.1525/elementa.195.f14

early and late summer haloclines shoaled at different rates following the YD 223 buoyancy and wind events. The early summer halocline immediately shallowed to 6 m while the late summer halocline slowly ascended to 8 m over the next 1.5 days (**Figure 15d**). Rapid shoaling of the early summer halocline placed the remnant mixed layer closer to the higher radiative fluxes near the surface (**Figure 15e**) and resulted in higher heat storage gains in the early summer case (**Figure 15f**).

To assess the sensitivity of the early summer case to wind forcing, we increased model winds by 50% resulting in an average wind of ~ 4 m s^{-1} and peak wind of 9 m s^{-1} (conditions similar to MIZ C2). Model results show that the early summer NSTM is cooler and deeper, but remains a distinctive feature in the upper 20 m of the modeled ocean (**Figure 16b**). This finding is in contrast to the late summer case which completely mixes out under the increased stresses with no temperature maximum or halocline present in the upper 20 m (**Figure 16c–d**). These findings suggest that the early summer halocline and NSTM is heavily buoyancy forced (melt pond drainage) and can develop over a board range of ice-ocean interface stresses.

5. Discussion

5.1 Summary of NSTM formation

In this study, we were able to successfully reproduce observed NSTMs in the early stages of development using the LTC 1-D turbulent boundary layer model. Model results showed that the increase in heat storage associated with development of the NSTM was largely due to the absorption of solar radiative fluxes just below the summer halocline stratification (**Figure 8**), consistent with the findings of Jackson et al. (2010) and Steele et al. (2011). Model results also showed that there was no evidence of vertical heat flux convergence through turbulent processes in the NSTM layer; however, the balance of turbulent momentum fluxes with buoyancy fluxes in the surface ocean had a large influence on the depth and strength of the summer halocline. The depth of the summer halocline is the most important factor for determining the amount of solar radiation absorbed in the NSTM layer (**Figure 15d–f**), while the strength of the protective summer halocline controls the amount of heat removed from NSTM by turbulent transport (**Figures 10** and **16**). The depth of the NSTM relative to the N^2 maximum was consistently deeper by 2–5 m (**Figures 8d** and **13a–b**). This greater depth was likely due to the higher levels of turbulence in the upper summer halocline, which were confirmed by eddy viscosity estimates from the LTC model (**Figure 8b**) and by observations from the Turbulence Frame (**Figure 11**). Even when turbulent eddies intermittently entered the NSTM layer, observations suggest the decrease in turbulent mixing length and intensity of these eddies strongly limited the amount of heat transported out of the NSTM layer (**Figure 11**). Overall, these findings suggest that the NSTM is dependent on the characteristics of the overlying summer halocline, which in turn is a function of the surface ocean shear and buoyancy production terms in the TKE balance.

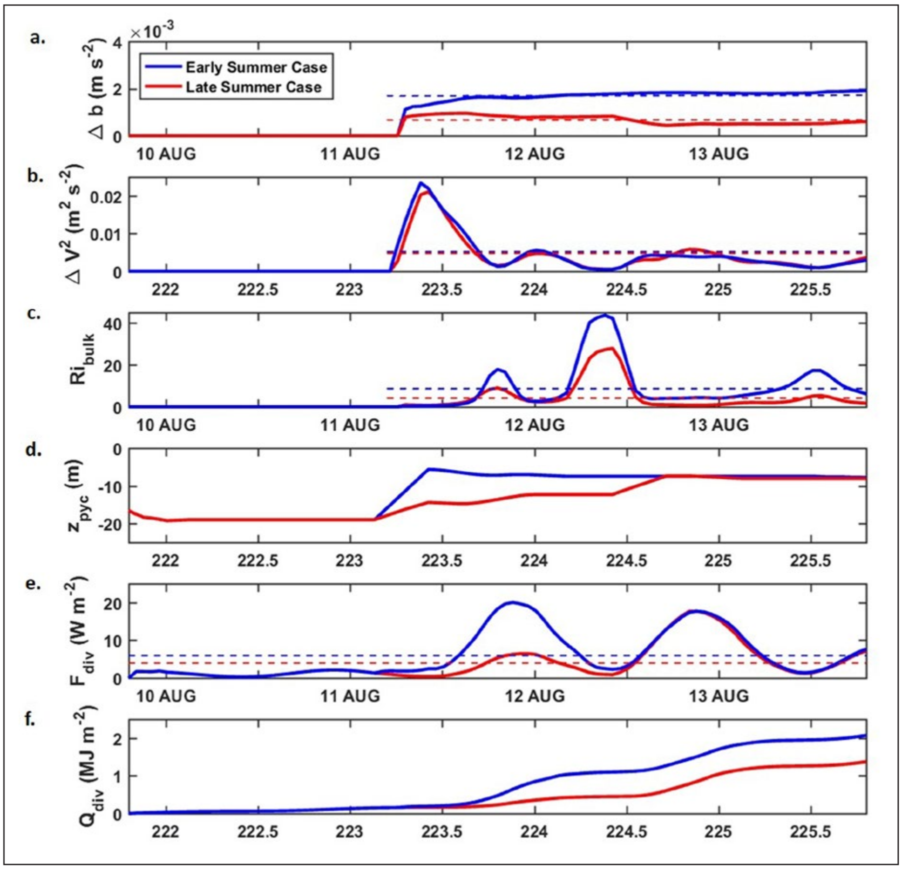

Figure 15: Plotted are the early (blue) and late (red) summer **(a)** buoyancy (Δb) and **(b)** shear (ΔV^2) components of the **(c)** bulk Richardson number (Ri_{bulk}) from the LTC model results presented on Fig. 14. Evaluation of the Ri_{bulk} and its components begin after the first buoyancy event on YD 223.1. Below these panels are the corresponding values of the **(d)** summer halocline depth (z_{pyc}), **(e)** the depth integrated absorbed solar flux below the summer halocline, and **(f)** the cumulative solar heat input below the summer halocline (Q_{div}). DOI: https://doi.org/10.1525/elementa.195.f15

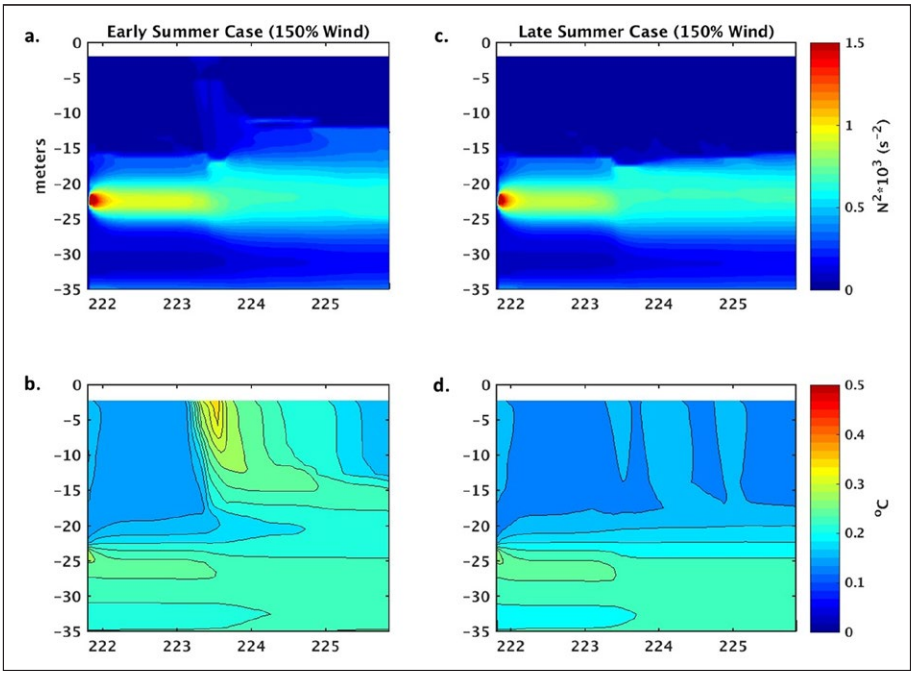

Figure 16: LTC model results of **(a, c)** N^2 and **(b, d)** δT for the high wind test (50% increase) conducted on the early **(a–b)** and late **(c–d)** summer NSTM using the air-ice-ocean conditions from MIZ C5. DOI: https://doi.org/10.1525/elementa.195.f16

5.2 Survivability of the early and late summer NSTM

These comprehensive observations from early and late summer allowed us to investigate the similarities and differences between the two NSTM events. The results of this study show that NSTM formation mechanisms were similar; however, the differences in early and late summer buoyancy forcing affected the intensity and survivability of the NSTM signal.

In early summer, the drainage of melt ponds substantially increased the strength of the summer halocline and increased the survivability of the NSTM. These conditions made formation of the early summer NSTM virtually inevitable, as it would have taken a strong storm event to erode the summer halocline stratification (**Figure 16a–b**) in this high Richardson number environment (**Figure 13e**). Comparison of the early and late summer NSTMs shows that the early summer case heats nearly twice as fast as the late summer case during initial development (**Figure 15f**). This enhanced heating was a consequence of the rapid shallowing by the surface mixed layer in response to strong buoyancy fluxes, which brings the residual mixed layer closer to the solar source (**Figure 15d–e**). Furthermore, the strength of the early summer halocline reduces the number of turbulent events that can penetrate the NSTM layer, allowing it to continue to accumulate solar input. The survivability of this accumulated heat storage is well documented (Jackson et al., 2010; Steele et al., 2011; Jackson et al., 2012; Timmermans, 2015) and confirmed in the late summer observations of this study (**Figure 3**). Along with the initial buoyancy increases provided by melt pond drainage, the persistence of the early summer halocline allows basal meltwater to be stored in the thin surface mixed layer and further enhances summer halocline stratification. In addition to these processes, Ekman pumping in the Canada Basin (Proshutinsky et al., 2009) adds additional freshwater to the summer mixed layer and deepens the NSTM further from ice-ocean interface stresses. These well-timed seasonal events in the ice-ocean system ensure development and preservation of the early summer NSTM which can then be a source of heat to the fall/winter ice-ocean boundary layer.

In late summer, the limited freshwater inputs from the sea ice greatly reduced the strength of the summer halocline and survivability of the NSTM. Freshwater fluxes were generally constrained to the collection of freshwater in leads due to lateral melt (Paulson and Pegau, 2001; Hayes and Morison, 2008), and basal melt due to ocean-to-ice heat fluxes. Basal melt rates during the MIZ-KOPRI Ice Camp were small (LTC model melt rate at C5 was ~ 0.7 cm day^{-1}) due to the large areal coverage of sea ice, low melt pond fraction, light winds, and reduced solar input in late summer. However, 6 cm of freshwater was introduced to the boundary layer prior to NSTM formation and was likely a result of meltwater mixed down from the surrounding leads during the YD 223.4 wind event. This wind effect is consistent with SHEBA observations and model studies which show that the surface fresh layers of leads mix out when winds increase to 6–7 m s^{-1} and wind stress approaches 0.1 N m^{-2} (Skyllingstad et al., 2005). In addition to freshening from above, observations and model results show that salt was entrained upward from the early summer halocline (**Figure 7d**), which further tightened the near-surface isohalines (**Figure 4b**). This further tightening suggests that the presence of the deeper early summer halocline may have assisted development of the late summer halocline. Nevertheless, the large disparity between early and late summer freshwater inputs made the late summer halocline and NSTM a marginally stable system. These results suggest that the late summer halocline and NSTM are transient features that can only be sustained during periods of weak winds.

6. Conclusions

Although the late summer NSTM was admittedly inconsequential from a heat storage perspective, the timely development of this feature within a comprehensive set of ice-ocean sensors provided an excellent laboratory for studying NSTMs in general. This study shows that a weak late summer NSTM can develop over a deeper, established, early-summer NSTM during weak wind conditions. As found in previous studies, our results show that the primary source of heating to the NSTM layer is penetrating solar radiation. However, the major findings of this study focus on the less studied background conditions that facilitate NSTM formation and the turbulent boundary layer processes that sustain or erode the NSTM.

Results from this study show that summer season buoyancy and wind events within the Canada Basin air-ice-ocean system facilitate the development of shallow haloclines and NSTMs. In early summer, rapid melt pond drainage supplies the buoyancy required to support the immediate development of the early summer halocline. The substantial buoyancy forcing provided by this meltwater generates a high Richardson number environment in the summer halocline that is able to endure elevated levels of ice-ocean interface stresses. Numerical model results show that the early summer NSTM continues to survive despite wind increases of 50% above the observed conditions. Furthermore, the strength of the early summer halocline prevents substantial turbulent fluxes from transporting heat out of the NSTM layer and ensures its survivability into late summer and fall.

In late summer, freshwater fluxes from the sea ice decrease considerably; however, during periods of weak winds, shallower haloclines may form above the early summer halocline. However, the weaker freshwater inputs in late summer permit only gradual shoaling of the surface mixed layer resulting in a 50% reduction in NSTM warming during initial development. The late summer halocline was less protective and permitted turbulent eddies to penetrate the NSTM layer, even during weak wind forcing. However, turbulence measurements from inside the late summer halocline and NSTM suggest that these turbulent eddies contracted in size and intensity and were not energetic enough to transport significant amounts of heat out of the NSTM layer. Wind and buoyancy sensitivity studies showed that the late summer NSTM was easily mixed out by wind increases above observed conditions even when buoyancy forcing was increased by 50%. These results show that the reduced availability of freshwater makes the late summer balance between interfaces stresses and buoyancy tenuous, and the survival of the late summer NSTM primarily dependent on local wind conditions.

Overall, the magnitude and fate of the NSTM depends on the strength and depth of the protective overlying summer halocline and wind forcing. The observations from MIZ cluster 5 show that multiple NSTMs can form and store heat in the Canada Basin upper ocean; however, the observations of Gallaher et al. (2016) and the numerical simulations of this study suggest that most of this heat resides in the early summer NSTM which forms following the drainage of melt ponds. This buoyancy event generates the persistent multi-seasonal summer halocline which acts as a mechanism for delivering summer absorbed solar heat to the fall/winter surface mixed layer and potentially delaying the onset of freezing.

Data accessibility statement
MIZ data available online: http://www.apl.washington.edu/project/project.php?id=miz.

Acknowledgements
We would like to thank Jim Stockel for his extensive contributions to the software development and assembly of the NPS Turbulence Frame. We would also like to thank the Korea Polar Research Institute for hosting the MIZ team onboard the R/V *Araon*. Declassified electro-optical imagery was made available by the U.S. intelligence community with assistance from Rob Graydon of Scitor Corporation. AWS data was provided by the Scottish Association of Marine Science and Ice-Tethered Profiler data was provided by the Woods Hole Oceanographic Institution. The MIZ experiment data were consolidated and made available by the University of Washington Applied Physics Lab (APL) on their collaboratory site (http://www.apl.washington.edu/project/project.php?id=miz).

Funding Information
This material is based upon research supported by, or in part by, the U.S. Office of Naval Research under award numbers N0001414WX20089 and N0001415WX01195. This work was partly supported by the K-AOOS (KOPRI, PM16040) Project funded by the Ministry of Oceans and Fisheries (MOF), South Korea.

Competing Interests
The authors have no competing interests to declare.

Contributions
- Contributed to conception and design: SGG, TPS
- Contributed to acquisition of data: SGG, TPS, WJS, S-HK, J-HK, K-HC
- Contributed to analysis and interpretation of data: SGG, TPS, WJS
- Drafted and/or revised the article: SGG
- Approved the submitted version for publication: SGG, TPS, WJS, S-HK, J-HK, K-HC

References
Comiso, JC, Parkinson, CL, Gersten, R and **Stock, L** 2008 Accelerated decline in the Artic sea ice cover. *Geophys Res Lett* **35**(1): DOI: https://doi.org/10.1029/2007GL031972

Fofonoff, NP and **Millard, RC** 1983 Algorithms for computations of fundamental properties of seawater. *Unesco Techincal Papers in Marine Science* **44**: 1–53.

Gallaher, SG, Stanton, TP, Shaw, WJ, Cole, ST, Toole JM, et al. 2016 Evolution of a Canada Basin ice-ocean boundary layer and mixed layer across a developing thermodynamically forced marginal ice zone. *J Geophys Res* **121**: 6223–6250. DOI: https://doi.org/10.1002/2016JC011778

Hayes, DR and **Morison, J** 2008 Ice-ocean turbulent exchange in the Arctic summer measured by an autonomous underwater vehicle. *Limnol Oceanogr* **53**(5, part 2): 2287–2308. DOI: https://doi.org/10.4319/lo.2008.53.5_part_2.2287

Hinze, JO 1975 *Turbulence*. New York: McGraw-Hill.

Jackson, JM, Allen, SE, McLaughlin, FA, Woodgate, RA and **Carmack, EC** 2011 Changes to the near-surface waters in the Canada Basin, Arctic Ocean from 1993–2009. *J Geophys Res* **116**(C10): 008. DOI: https://doi.org/10.1029/2011JC007069

Jackson, JM, Carmack, EC, McLaughlin, FA, Allen, SE and **Ingram, RG** 2010 Identification, characterization, and change of the near-surface temperature maximum in the Canada Basin. 1993-2008. *J Geophys Res* **115**(5): 1993–2008. DOI: https://doi.org/10.1029/2009JC005265

Jackson, JM, Williams, WJ and **Carmack, EC** 2012 Winter sea-ice melt in the Canada Basin, Arctic Ocean. *Geophys Res Lett* **39**(3): 2–7. DOI: https://doi.org/10.1029/2011GL050219

Kolmogorov, AN 1941 Dissipation of energy in a locally isotropic turbulence. *Dokl Akad Nauk SSSR* **32**: 141. (English translation in *Proc R Soc London A* 434: 15, 1991).

Krishfield, R, Toole, J, Proshutinsky, A and **Timmermans, M-L** 2008 Automated ice-tethered profilers for seawater observations under pack ice in all seasons. *J Atmos Oceanic Technol* **25**(11): 2091–2105. DOI: https://doi.org/10.1175/2008JTECHO587.1

Large, WG, McWilliams, JC and **Doney, SC** 1994 Oceanic vertical mixing: A review and a model with a nonlocal boundary layer parameterization. *Rev Geophys* **32**(4): 363–403. DOI: https://doi.org/10.1029/94RG01872

Lee, CM, Cole, ST, Doble, M, Freitag, L, Hwang, P, et al. 2012 Marginal Ice Zone (MIZ) Program: Science and experiment plan. Seattle, WA: Applied Physics Laboratory, University of Washington. Technical Report APL-UW 1201. http://www.apl.washington.edu/research/downloads/publications/tr_1201.pdf

Macdonald, RW, Carmack, EC, McLaughlin, FA, Falkner, KK and **Swift, JH** 1999 Connections among ice, runoff and atmospheric forcing in the Beaufort

Gyre. *Geophys Res Lett*, **26**(15): 2223–2226. DOI: https://doi.org/10.1029/1999GL900508

Maykut, GA 1985 An introduction to ice in polar oceans. Seattle, WA: Applied Physics Laboratory, University of Washington. Technical Report APL-UW 8510. http://oai.dtic.mil/oai/oai?verb=getRecord&metadataPrefix=html&identifier=ADA166140.

Maykut, GA and **McPhee, MG** 1995 Solar heating of the Arctic mixed layer. *J Geophys Res* **100**(C12): 24691–24703. DOI: https://doi.org/10.1029/95JC02554

McPhee, MG 1987 A time-dependent model for turbulent transfer in a stratified oceanic boundary layer. *J Geophys Res* **92**(C7): 6977–7986. DOI: https://doi.org/10.1029/JC092iC07p06977

McPhee, MG 1994 On the turbulent mixing length in the Oceanic Boundary Layer. *J Phys Oceanogr* **24**(9): 2014–2031. DOI: https://doi.org/10.1175/1520-0485(1994)024<2014:OTTMLI>2.0.CO;2

McPhee, MG 1998 Freshening of the upper ocean in the Arctic: Is perennial sea ice disappearing. *Geophys Res Lett* **25**(10): 1729–1732. DOI: https://doi.org/10.1029/98GL00933

McPhee, MG 1999 Scales of turbulence and parameterization of mixing in the ocean boundary layer. *J Mar Sys* **21**(1): 55–65. DOI: https://doi.org/10.1016/S0924-7963(99)00005-6

McPhee, MG 2002 Turbulent stress at the ice/ocean interface and bottom surface hydraulic roughness during the SHEBA drift. *J Geophys Res* **107**(C10): 1–15. DOI: https://doi.org/10.1029/2000JC000633

McPhee, MG 2008 *Air-Ice-Ocean Interaction: Turbulent Ocean Boundary Layer Exchange Processes*. 2nd ed., New York: Springer. DOI: https://doi.org/10.1007/978-0-387-78335-2

McPhee, MG and **Martinson, DG** 1994 Turbulent mixing under drifting pack ice in the Weddell Sea. *Science* **263**(5144): 218–221. DOI: https://doi.org/10.1126/science.263.5144.218

McPhee, MG, Proshutinsky, A, Morison, JH, Steele, M and **Alkire, MB** 2009 Rapid change in freshwater content of the Arctic Ocean. *Geophys Res Lett* **36**(10): L10602. DOI: https://doi.org/10.1029/2009GL037525

Paulson, CA and **Pegau, WS** 2001 The summertime thermohaline evolution of an Arctic lead: Heat budget of the surface layer. *In Proceedings of the Sixth Conference on Polar Meteorology and Oceanography*, American Meteorological Society: 271–274, San Diego, CA.

Perovich, DK, Light, B, Eicken, H, Jones, KF, Runciman, K, et al. 2007 Increasing solar heating of the Arctic Ocean and adjacent seas, 1979–2005: Attribution and role in the ice-albedo feedback. *Geophys Res Lett* **34**(19): 1–5. DOI: https://doi.org/10.1029/2007GL031480

Price, JF, Weller, RA and **Pinkel, R** 1986 Diurnal cycling: Observations and models of the upper ocean response to diurnal heating, cooling, and wind mixing *J Geophys Res* **91**(C7): 8411–8427. DOI: https://doi.org/10.1029/JC091iC07p08411

Proshutinsky, A, Krishfield, R, Timmermans, M-L, Toole, J, Carmack, E, et al. 2009 Beaufort Gyre freshwater reservoir: State and variability from observations. *J Geophys Res* **114**: C00A10. DOI: https://doi.org/10.1029/2008JC005104

Rudels, B, Jones, EP, Schauer, U and **Eriksson, P** 2004 Atlantic sources of the Arctic Ocean surface and halocline waters. *Polar Res* **23**(2): 181–208. DOI: https://doi.org/10.1111/j.1751-8369.2004.tb00007.x

Shaw, WJ, Stanton, TP, McPhee, MG and **Kikuchi, T** 2008 Estimates of surface roughness length in heterogeneous under-ice boundary layers. *J Geophys Res* **113**(C08): 030. DOI: https://doi.org/10.1029/2007JC004550

Skyllingstad, ED and **Paulson, CA** 2005 Simulation of turbulent exchange processes in summertime leads. *J Geophys Res* **110**(C05): 021. DOI: https://doi.org/10.1029/2004JC002502

Steele, M, Ermold, W and **Zhang, J** 2008 Arctic Ocean surface warming trends over the past 100 years. *J Geophys Res Lett* **35**(2): L02614. DOI: https://doi.org/10.1029/2007GL031651

Steele, M, Ermold, W and **Zhang, J** 2011 Modeling the formation and fate of the near-surface temperature maximum in the Canada Basin of the Arctic Ocean. *J Geophys Res* **116**(C11): C11015. DOI: https://doi.org/10.1029/2009JC006803

Steele, M, Zhang, J and **Ermold, W** 2010 Mechanisms of summertime upper Arctic Ocean warming and the effect on sea ice melt. *J Geophys Res* **115**: C11004. DOI: https://doi.org/10.1029/2009JC005849

Taylor, GI 1938 The Spectrum of Turbulence. *Proc R Soc London A* **164**: 476. DOI: https://doi.org/10.1098/rspa.1938.0032

Timmermans, M-L 2015 The impact of stored solar heat on Arctic sea ice growth. *Geophys Res Lett* **42**(15): 6399–6406. DOI: https://doi.org/10.1002/2015GL064541

Timmermans, M-L, Cole, ST and **Toole, JM** 2012 Horizontal density structure and restratification of the Arctic Ocean surface layer. *J Phys Oceanogr* **42**: 659–668. DOI: https://doi.org/10.1175/JPO-D-11-0125.1

Toole, JM, Krishfield, RA, Timmermans, M-L, Proshutinsky, A 2011 The Ice-Tethered Profiler: ARGO of the Arctic. *Oceanography* **24**(3): 162–173. DOI: https://doi.org/10.5670/oceanog.2011.65

Toole, JM, Timmermans, M-L, Perovich, DK, Krishfield, RA, Proshutinsky, A, et al. 2010 Influences of the ocean surface mixed layer and thermohaline stratification on Arctic Sea ice in the central Canada Basin. *J Geophys Res* **115**(10): 1–14. DOI: https://doi.org/10.1029/2009JC005660

Untersteiner, N 1961 On the mass and heat budget of Arctic sea ice. *Arch Meteorol Geophys Bioklimatol Ser A* **12**: 151–182. DOI: https://doi.org/10.5670/oceanog.2011.65

Vancoppenolle, M, Fichefet, T and **Bitz, CM** 2006 Modeling the salinity profile of undeformed Arctic sea ice. *Geophys Res Lett* **33**(21): L21501. DOI: https://doi.org/10.1029/2006GL028342

Yamamoto-Kawai, M, McLaughlin, FA, Carmack, EC, Nishino, S, Shimada, K, et al. 2009 Surface freshening of the Canada Basin, 2003–2007: River runoff versus sea ice meltwater. *J Geophys Res.* **114**(C1): C00A05. DOI: https://doi.org/10.1029/2008JC005000

How to cite this article: Gallaher, S G, Stanton, T P, Shaw, W J, Kang, S-H, Kim, J-H and Cho, K-H 2017 Field observations and results of a 1-D boundary layer model for developing near-surface temperature maxima in the Western Arctic. *Elem Sci Anth,* 5: 11, pp. 1–21, DOI: https://doi.org/10.1525/elementa.195

Domain Editor-in-Chief: Jody W. Deming, University of Washington

Guest Editor: Craig M. Lee, University of Washington

Knowledge Domain: Ocean Science

Part of an *Elementa* Special Feature: Marginal ice zone processes in the summertime Arctic

Submitted: 13 August 2016 **Accepted:** 19 December 2016 **Published:** 22 March 2017